Master Thesis

Dispersion Measurements and Frequency Comb Generation in A Si_3N_4 Microring Resonator

Caroline Munck Nielsen

Dispersion Measurements and Frequency Comb Generation in A Si_3N_4 Microring Resonator

Author	Caroline Munck Nielsen
Advisor:	Associated Professor Jörg Helge Müller
Advisor:	Asbjørn Arvad Jørgensen
Advisor:	Martin Romme Henriksen
Advisor:	Professor Jan Westenkær Thomsen

Quantum Metrology Group
The Niels Bohr Institute

Submitted to the University of Copenhagen
December 3, 2020

Abstract

The spectra of an optical frequency combs consist of a series of equally spaced lines covering a wide area of frequencies which makes it useful for a variety of applications. Each of the lines in such a comb can be used as a reference source for measuring absolute optical frequencies. Chip-based microresonators have paved the way for a new innovative way of generating frequency combs based on nonlinear processes on a compact scale.

In this in work we measure the dispersion and characterise the behaviour of a Si_3N_4 microring resonator for the purpose of frequency comb generation. For the characterisation of the device, we propose a setup using a free-space cavity allowing for a near dispersion-free reference. The device was shown to have an FSR of 100.2882 ± 0.0001 GHz with the anomalous dispersion needed for comb generation.

The formation of solitons is observed through the soliton trace signal. We investigate the dynamics and formation of optical solitons in the aforementioned microresonator by looking at how the trace signal depends on parameters such as the resonance frequency and on-chip power. Finally, frequency comb generation is demonstrated under the different conditions and their performance is compared. We found a strong correlation between on-chip power and the total soliton step length. The best results were obtained when pumping the microresonator around 1550 nm. Here, we observed the longest total soliton step lengths and generated the widest frequency combs.

Acknowledgment

This thesis was a long time coming and there are many people whom I own my thanks to.

First of all, I would like to thank professor Jan W. Thomsen who have been a great supervisor for the first many months. Your questions and ideas were always welcome and highly appreciated. Next, I want to thank Associate Professor Jörg H. Müller for stepping in and taking over for Jan in the last months of my thesis. You have been of greater help than you think.

Secondly, I need to extend my deepest gratitude to my supervisors Asbjørn A. Jørgensen and Martin R. Henriksen. They have both been very patient and have taken their time to explain and teach me so many things, and I feel I have come a long way since I started. Same goes for the rest of the Quantum Metrology group at the Niels Bohr Institute. It has been a pleasure working alongside you guys. I am really going to miss all the fun in the lab and all our (very) long coffee breaks in the lounge.

A special thanks to my boyfriend Andreas for putting up with me in stressed times and for always supporting me and cheering me on. I would also thank the rest of my family and friends for always being willing to help with whatever has been needed.

Thank you to Maria, Bastian, Anton, and Lasse for being the most amazing office mates I could possibly think of - we definitely deserve the title 'Office of the year'.

Finally, I would like to thank the people who have been reading through partly finished chapters - especially thanks to Julian for trying to teach me the comma rules.

Contents

List of Figures

Chapter 1

Introduction

1.1 Optical Frequency Combs

Back in 2005 John L. Hall and Theodor W. Hänsch aroused interest in scientists world over when their work within optical frequency combs (OFC) was awarded half a Nobel Prize. Since then, the importance and applicability of OFCs has been recognised by many who now work to achieve a better understanding of how they work and how to approve their performances even further.

The term *frequency comb* is used to describe a spectrum consisting of equidistant lines in the frequency domain which in the time domain translates into a periodic train of pulses with a repetition rate of f_r. This repetition rate corresponds to the spacing between the comb lines in the frequency domain. Due to the equidistant spacing of the comb lines the frequency comb can be used as an optical ruler to measure the unknown frequencies by measuring the beat note between the two sources. This of course implies that the frequency of each comb line is well known.

In an ideal scenario the pulse train would be perfectly periodic, however, in the real world, the spectrum will often be shifted from zero by an offset in frequency, called the carrier-envelope offset, f_{ceo}. In the time domain, this corresponds to an evolution in the phase of the carrier-envelope [17]:

$$f_{ceo} = f_r \frac{\Delta\phi}{2\pi}, \tag{1.1}$$

where $\Delta\phi = \phi_2 - \phi_1$ is the difference in the carrier envelope phase between two consecutive pulses. The frequency of each comb line can be defined according to the repetition rate and the carrier-envelope offset with respect to the mode number:

$$f_n = nf_r + f_{\text{ceo}}. \tag{1.2}$$

There are several methods to achieve a frequency comb structure and they can be divided into three classes based on the experimental techniques used for generation.

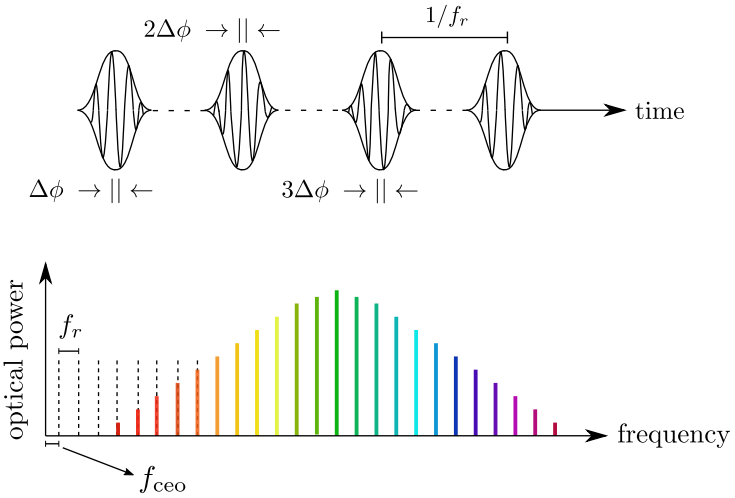

Figure 1.1: Representation of a frequency comb in the time and frequency domain: (**top**) pictures a pulse train with a repetition rate of $1/f_r$ and a phase-shift $\Delta\phi$. (**bottom**) The fourier transform of the of the pulse train leads to the comb structure in the frequency domain. The frequency comb consists of several equidistant lines with a spacing equal to f_r.

The first frequency combs that were developed were based on mode-locked lasers (MLL). Today, it still remains the most commonly used method of frequency comb generation. A mode-locked laser utilises a broad gain medium that, when put in a laser cavity, can be used to excite several cavity modes. If the cavity modes are phase-locked they will appear as short pulse circulating inside the cavity. The repetition rate of the pulses corresponds to the length of the optical path of such laser cavity. Typically, the repetition rate of an MLL comb is between 100 MHz and a couple of GHz [6] [4].

Frequency combs can also be generated through electro-optic modulation of a continuous wave (CW) laser by modulation of either the amplitude or the phase. The modulation creates sidebands on each side of the CW laser. Compared to MLL generated frequency combs, higher repetition rates can be achieved using EO modulation. The repetition rate can reach up to 10 GHz but the number of comb lines obtained is much lower [5].

Lastly, there is frequency comb generation using microresonators. The progress within development of nano-structure have paved the road for chip-based frequency combs. These combs have the advantage that they can be integrated onto platforms making them compact in size and cheaper to produce compared to the other types of frequency combs.

1.1.1 Frequency Comb Generation in Microresonators

The topic of this thesis is microresonator based frequency comb, commonly referred to as a micro-comb. These combs are generated through the nonlinear optical

process known as four wave mixing (FWM).

Microresonators come in several shapes and can be made of a variety of different nonlinear materials. Figure 1.2 shows different examples of device shapes.

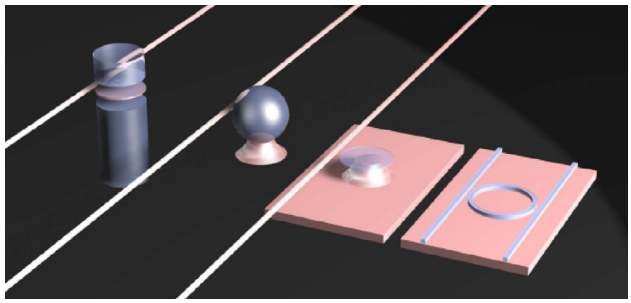

Figure 1.2: Microresonators with different types of geometry. From the left; cylindrical, spherical, toroidal, and ring. The image is adapted from [19].

The cylindrical, spherical, and toroidal shape microresonators are based on the are typically referred to as whispering-gallery mode (WGM) resonators, whereas the ring shaped microresonator (microring resonator) is an integrated monolithic device based on total internal reflection [19].

The purpose of this thesis is to demonstrate and investigate frequency comb generation in a silicon nitride (SiN) microring resonator (MRR) through experiments carried out in the laboratory, as well as providing the reader with a general understanding of the fundamental theory and dynamics of frequency comb generation in microresonators.

Overview

Chapter 2 goes through the basic theory of wave propagation in waveguides by first deriving the nonlinear Schrödinger equation for a straight waveguide, and thereafter adapting it to apply to a ring-shaped resonator.

Chapter 3 describes the different dynamics involved in the generation of a frequency comb in a MRR and how they are related. A brief description is given on the fabrication process of MRR and lastly we present the device we have been working on.

In **Chapter 4** we present our results for the characterisation of the dispersion of the SiN MRR device, and we discuss different characterisation techniques.

Chapter 5 is about the formation of optical soliton in MRRs and how frequency combs are generated in such devices. We investigate the dependencies of the total soliton step length and present and compare the experimentally generated frequency combs in the SiN device using two different lasers.

Chapter 6 investigates the frequency stability of the experimentally generated combs.

Chapter 2

Propagation of Light in Optical Waveguides

2.1 Pulse Propagation

The propagation of electromagnetic waves in dielectric isotropic materials can be described through Maxwell's equations[1]:

$$\nabla \times \mathbf{E}(\mathbf{r},t) = -\frac{\partial \mathbf{B}(\mathbf{r},t)}{\partial t}, \qquad (2.1a)$$

$$\nabla \times \mathbf{H}(\mathbf{r},t) = \frac{\partial \mathbf{D}(\mathbf{r},t)}{\partial t}, \qquad (2.1b)$$

$$\nabla \cdot \mathbf{B}(\mathbf{r},t) = 0, \qquad (2.1c)$$

$$\nabla \cdot \mathbf{D}(\mathbf{r},t) = 0. \qquad (2.1d)$$

For nonmagnetic materials the constitutive relations are given by the displacement vector field $\mathbf{D}(\mathbf{r},t) = \epsilon_0 \mathbf{E}(\mathbf{r},t) + \mathbf{P}(\mathbf{r},t)$ and the magnetic field $\mathbf{B}(\mathbf{r},t) = \mu_0 \mathbf{H}(\mathbf{r},t)$. Taking the curl of $\nabla \times \mathbf{E}$ and inserting the expression for $\mathbf{H}(\mathbf{r},t)$ and $\mathbf{D}(\mathbf{r},t)$ the equation becomes

$$\nabla \times \nabla \times \mathbf{E}(\mathbf{r},t) = -\left(\frac{1}{c^2}\epsilon_0 \frac{\partial^2 \mathbf{E}(\mathbf{r},t)}{\partial t^2} + \mu_0 \frac{\partial^2 \mathbf{P}(\mathbf{r},t)}{\partial t^2}\right). \qquad (2.2)$$

Following the approach of [2] and [23] the polarisation can be rewritten in order to include the nonlinear interactions between light and matter in the materials. This is done using a perturbation series, $\mathbf{P}(\mathbf{r},t) = \sum_{k=1}^{\infty} \mathbf{P}^{(k)}(\mathbf{r},t)$ that is inserted into Eqn. (7.2) which then becomes the nonlinear wave equation in the time domain,

$$\nabla\times\nabla\times\mathbf{E}(\mathbf{r},t)+\frac{1}{c^2}\frac{\partial^2}{\partial t^2}\int_{-\infty}^{\infty}\left(1+\chi^{(1)}\right)\mathbf{E}(\mathbf{r},\omega)e^{-i\omega t}d\omega = -\mu_0\frac{\partial^2}{\partial t^2}\mathbf{P}^{(\mathrm{NL})}(\mathbf{r},t). \qquad (2.3)$$

[1] A more detailed derivation can be found in Appendix A

$\mathbf{P}^{(\mathrm{NL})}(\mathbf{r},t) = \sum_{k=2}^{\infty} \mathbf{P}^{(k)}(\mathbf{r},t)$ is the nonlinear induced polarization and $\chi^{(1)}$ is the first order susceptibility which is related to the polarisation and the electric field through $\mathbf{P} = \epsilon\chi\mathbf{E}$. In the frequency domain Eqn. (7.3) translates into,

$$-\nabla^2\mathbf{E}(\mathbf{r},\omega) = \frac{\omega^2}{c^2}\mathbf{E}(\mathbf{r},\omega) + \mu_0\omega^2\mathbf{P}(\mathbf{r},\omega), \tag{2.4}$$

where we have used the vector identity $\nabla \times \nabla \times E = -\nabla^2 E$ assuming that the material is homogeneous.

In the time domain, the field of quasi-monochromatic waves consists of one or more carrier waves multiplied with a slowly varying envelope (see Figure 2.1),

$$E(r,t) = \frac{1}{2}\left(E^0_{\omega_\sigma}(r,t)e^{-i\omega_\sigma t} + c.c\right). \tag{2.5}$$

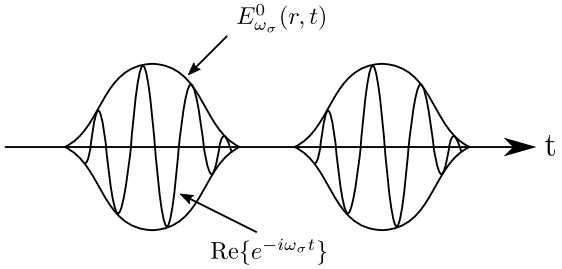

Figure 2.1: Illustration of a quasi-monochromatic wave.

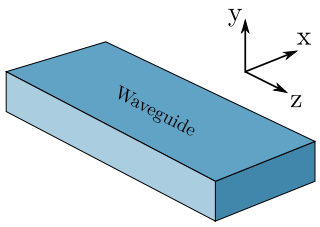

Figure 2.2: Waveguide with propagation in the z-direction. The cross section defined by the coordinates x, y.

The nonlinear wave equation can be derived for a field propagating in a homogeneous waveguide by assuming that the amplitude of the field can be separated into an envelope $\mathcal{A}(\omega - \omega_\sigma)$ and a radial distribution $R(x,y)$,

$$E_{\omega_0}(\mathbf{r},\omega-\omega_0) = \mathcal{A}(\omega-\omega_0)R(x,y)e^{i\beta_0 z}. \tag{2.6}$$

Writing the linear and nonlinear induced polarization as separate fields in a similar form as the electric field in Eqn. (7.5) and only considering the positive frequencies, the nonlinear wave equation becomes:

$$\left(\nabla^2 + \frac{\omega^2}{c^2}\left(1+\chi^{(1)}\right)\right)E^0_{\omega_0}(\mathbf{r},\omega-\omega_0) = -\mu_0\omega^2(P^0_{\omega_0})^{NL}(\mathbf{r},\omega-\omega_0). \tag{2.7}$$

The induced polarisation can be written as an effective linear polarisation, $\left(P^0_{\omega_0}\right)^{NL}(\mathbf{r},\omega-\omega_0) = \epsilon_0 K\chi^{(3)}E_{\omega_1}E_{\omega_2}E_{\omega_3} = \epsilon_0\tilde{\chi}^{(1)}E^0_{\omega_0}$, where $\tilde{\chi}^{(1)}$ is an effective first order susceptibility. Eqn. (7.7) can then be rewritten using the electric field from Eqn. (7.5):

$$\left[-\nabla^2_\perp R(x,y) + \frac{\omega^2}{c^2}(1+\chi^{(1)}+\tilde{\chi}^{(1)})R(x,y)\right]\frac{1}{R(x,y)} = \frac{1}{\mathcal{A}e^{i\beta_0 z}}\nabla^2_z(\mathcal{A}e^{i\beta_0 z}). \tag{2.8}$$

By separating the radial and longitudinal dependencies the RHS now only depends on the cartesian coordinates $\mathbf{r} = (x, y)$ and the LHS only depends on z. By setting both sides equal to a constant $\tilde{\beta}^2$ the two equations can be solved. Considering a waveguide with a perturbation can show that a perturbation in the relative permittivity will lead to a change in the propagation constant when solving for the radial part:

$$\Delta\beta = \frac{k_0^2}{2\beta_0} \frac{\int_A \tilde{\chi}^{(1)} |R(x,y)|^2 da}{\int_A |R(x,y)|^2 da}, \tag{2.9}$$

where the integral is performed over the cross sectional area of the waveguide. For a wave propagating in the z-direction, the propagation equation can be written as a complex-valued slowly-varying envelope function of the electric field. Applying the slowly varying wave approximation the propagation equation in the time domain can be written as:

$$\frac{\partial A}{\partial z} + \beta_1 \frac{\partial A}{\partial t} + i\frac{1}{2}\beta_2 \frac{\partial^2 A}{\partial t^2} - i\Delta\beta A = 0, \tag{2.10}$$

where β_1 is the inverse group velocity v_g^{-1}, β_2 is the group velocity dispersion (GVD) and $\Delta\beta$ is the change in the propagation constant.

Light that is propagating through a waveguide will be subject to dispersion through the intensity dependent refractive index (Kerr refractive index). This is accounted for by writing the change in the propagation constant as:

$$\Delta\beta = \frac{\omega n_2^I}{c} \frac{P}{A_{\text{eff}}}, \tag{2.11}$$

with n_2^I being the intensity dependent refractive index, P the power, and A_{eff} the effective cross sectional area. This allows for the last term on the LHS in Eqn. (2.10) to be rewritten as:

$$i\Delta\beta A = i\gamma |A|^2 A, \tag{2.12}$$

where $P = |A|^2$ and $\gamma = 2\pi n_2 / \lambda A_{eff}$. Lastly, introducing a coordinate system that moves with the group velocity such that $\beta_1 = 1/v_g$ Eqn. (2.10) reduces to:

$$\frac{\partial A}{\partial z} + i\frac{1}{2}\beta_2 \frac{\partial^2 A}{\partial t^2} - i\gamma |A|^2 A = 0. \tag{2.13}$$

This equation is known as the *Nonlinear Schrödinger Equation* (NLSE). The second term on the RHS is responsible for the group velocity dispersion (GVD) and the last term on the RHS is the term responsible for the nonlinearity (the Kerr effect).

In a lossy waveguide the intrinsic loss, α, can be accounted for by adding an extra term. The term can be included in $\Delta\beta$ by substituting:

$$\Delta n = n_2 |E|^2 \rightarrow \Delta n = n_2 |E|^2 + \frac{i}{2k_0}\alpha, \tag{2.14}$$

which then arises in the expression for $\Delta\beta$ as:

$$\Delta\beta = \frac{\omega}{c}\left(n_2^I \frac{P}{A_{eff}} + i\alpha\right) \tag{2.15}$$

Including this extra term in the NLSE the equation then becomes:

$$\frac{\partial A}{\partial z} + \frac{i}{2}\beta_2 \frac{\partial^2 A}{\partial t^2} - i\gamma|A|^2 A + \frac{\alpha}{2} = 0. \tag{2.16}$$

The NLSE is a fundamental equation for studying the nonlinear effects in waveguides. It is especially useful for the study of optical solitons and their behaviour in optical waveguides. The two versions of the equation presented in Eqn. (2.13) and Eqn. (7.38) are the most simplest forms of the equation used to describe third order nonlinear effects. They can however be modified to include other nonlinear effects, such as the Raman effect or self-steepening, as well as higher order terms.

2.2 Optical Fields in a Ring Resonator

Optical microring resonators (MRRs), like the one that we have used for our experiments, are waveguides closed to form a loop usually in the shape of a ring or a racetrack. These MRRs act as travelling wave resonators. Light is coupled in and out of the MRR via a straight bus waveguide through a phenomenon known as evanescent coupling. In order for the light to couple from the bus waveguide and into the MRR it must match a resonance of the MRR. The light that then propagates inside of the ring-shaped waveguide will interfere with itself after each roundtrip which can lead to a large intensity build-up inside the MRR.

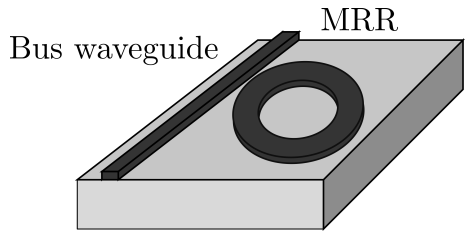

Figure 2.3: A typical all-pass type MRR consisting of a circular microring and a straight bus waveguide.

There are two types of configurations that are commonly used for the coupling of light into the MRR: (1) add-drop and (2) all-pass. An illustration of an all-pass type MRR (coupled to a single bus waveguide) is shown in Figure 2.3. This type of MRR is what we used for our experiments. A typical all-pass microring resonator consists of a bus waveguide and a ring shaped wave-guide of length L acting as a ring resonator as depicted in Fig. (2.4). The close placement of the ring-shaped

waveguide and the straight bus waveguide allows for evanescent coupling between the two when the input electric fields matches a cavity resonance.

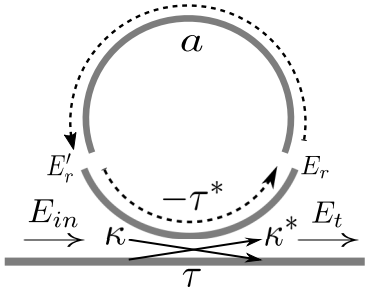

Figure 2.4: Optical fields in an all-pass microring resonator.

Following a similar approach as the one in [**?**], the relations between the input field E_{in}, the transmitted field E_t, and the circulating fields E_r and $E_r^{'}$ can be derived by combining the relations of the coupling and transmission coefficient. Mathematically, the transmission and coupling of an all-pass microring resonator is described through the matrix[2]:

$$\begin{bmatrix} E_t \\ E_r \end{bmatrix} = \begin{bmatrix} \tau & \kappa \\ -\kappa^* & \tau^* \end{bmatrix} \begin{bmatrix} E_{in} \\ E_r^{'} \end{bmatrix}, \tag{2.17}$$

where κ is the coupling coefficient describing the coupling strength and τ is the transmission coefficient describing transmission between the bus waveguide and the ring resonator. Both κ and τ are complex numbers. We assume that $|\tau|^2+|\kappa|^2 = \beta$ where the case of $\beta = 1$ corresponds to a lossless coupling to the resonator. From Eqn. (2.17) we get the two relations:

$$\begin{aligned} E_t &= \tau E_{in} + \kappa E_r^{'}, \\ E_r &= \tau^* E_r^{'} - \kappa^* E_{in}. \end{aligned} \tag{2.18}$$

The light entering into the cavity, E_r, can be related to the light measured at the coupling point after a roundtrip by:

$$E_r^{'} = a e^{i\theta} E_r, \tag{2.19}$$

where a is a real number describing the internal loss and θ is the roundtrip phase. When $a = 1$ there are no internal losses in the resonator. Combining Eqn. (2.18) and Eqn. (2.19) results in:

$$E_r^{'} = E_{in}\left(\frac{-\kappa^* a}{-a\tau^* + e^{-i\theta}}\right), \tag{2.20}$$

[2]Note that the τ in this section has been chosen to conform with other literature on the subject but it is not the same τ used in other parts of this project.

$$E_t = E_{in}\left(\frac{-a\beta + \tau e^{-i\theta}}{-a\tau^* + e^{-i\theta}}\right), \tag{2.21}$$

where $E_r^{'}$ is the field circulating inside the resonator at the coupling point and E_t is the transmitted field at the output port. The power transmission of the output port is given by:

$$T = \frac{|E_t|^2}{|E_{in}|^2} = \frac{\beta^2 a^2 + |\tau|^2 - 2a\beta|\tau|cos(\theta + \phi_\tau)}{1 + a^2|\tau|^2 - 2a|\tau|cos(\theta + \phi_\tau)}, \tag{2.22}$$

where $\tau = |\tau|e^{i\phi_\tau}$. At resonance $\theta + \phi_\tau = 2\pi m$, with $m = 1, 2, ..., n$, the transmission through the MRR follows the relation:

$$T = \frac{(a\beta - |\tau|)^2}{(1 - a|\tau|)^2}. \tag{2.23}$$

The transmission function T for an all-pass MRR can be seen in Figure 2.5 for the parameters $\tau = 0.75$, $\beta = 1$ and varying losses a as a function of normalised detuning ϕ:

$$T = \frac{a^2 + |\tau|^2 - 2a|\tau|cos(\phi)}{1 + a^2|\tau|^2 - 2a|\tau|cos(\phi)}. \tag{2.24}$$

Critical coupling occurs when equals $\tau = a$ which can be seen by the function dropping to zero at $\phi = 0$. This is the special case where the losses of the microresonator is precisely balanced by the light that is coupled into the microresonator. The microresonator is said to be undercoupled when the losses are greater than the coupling which corresponds in the figure to $a > 0.75$. Overcoupling happens when there is more light coupling into the microresonator than is lost. In the special case $a = 1$, corresponding to a perfect lossless case, all light is transmitted.

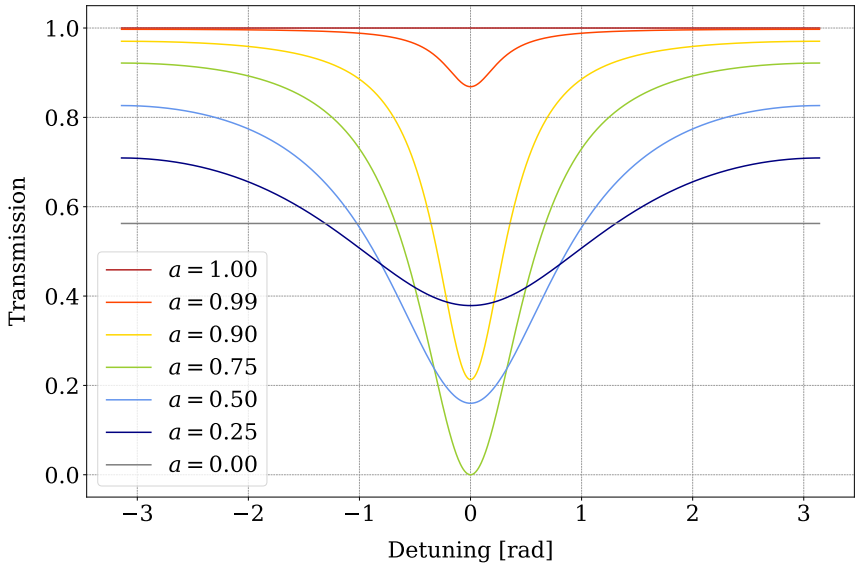

Figure 2.5: The transmission function T as a function of cavity detuning ϕ for different losses a and $\tau = 0.75$.

A ring resonator is typically characterized using four parameters, two of which can be derived from the other: free spectral range (FSR), finesse F, full width half maximum (FWHM), and quality factor (also referred to as Q-value) Q.

Free Spectral Range: The FSR is defined as the distance between two peaks of resonance. The resonances appear at those frequencies at which constructive interference is present after one roundtrip inside the cavity. In a classic Fabry-Pérot interferometer (free space cavity) the FSR is typically expressed in terms of frequency as:

$$\Delta\nu_{FSR} = \frac{c}{2nL}, \tag{2.25}$$

with n being the refractive index and L the length of the cavity. In the case of a ring resonator the FSR can be obtained from the propagation constant β [21]:

$$\Delta\lambda_{\mathrm{FSR}} = \frac{2\pi}{L}\left|\frac{\partial\beta}{\partial\lambda}\right|^{-1}, \tag{2.26}$$

or, similarly:

$$\Delta\nu_{\mathrm{FSR}} = \frac{2\pi}{L}\left|\frac{\partial\beta}{\partial\nu}\right|^{-1}. \tag{2.27}$$

From the resonant condition for $\beta = 2\pi n_{eff}/\lambda$ the FSR becomes:

$$\Delta\lambda_{\mathrm{FSR}} = \frac{\lambda^2}{n_{eff}L}. \tag{2.28}$$

Taking the chromatic dispersion of a waveguide into account would lead to a more precise expression. By introducing the group refractive index n_g:

$$\Delta\beta/\Delta\lambda = -kn_g, \quad n_g = n_{eff} - \lambda\frac{\partial n_{eff}}{\partial\lambda}, \tag{2.29}$$

will then lead to the final expression with the dispersion of the resonator taken into account:

$$FSR = \Delta\lambda = \frac{\lambda^2}{n_g L}. \tag{2.30}$$

FWHM: The FWHM is defined as the full spectral width of the resonance at half the maximum. In the case of an all-pass type ring resonator the FWHM is sometimes instead defined as the full width at half depth (FWHD) [**?**]:

$$FWHM \approx \frac{\lambda^2\kappa^2}{4\pi^2 n_g R}, \tag{2.31}$$

κ is the optical resonance coupling frequency and R is the radius of the ring resonator.

Finesse The ratio between the FSR and the FWHD defines the finesse of the resonator:

$$\mathcal{F} = \frac{FSR}{FWHD} \approx \frac{2\pi}{\kappa^2}. \tag{2.32}$$

Q-Value The last parameter, the Q-value, describes the dampening of a resonator. It represents how sharp a resonance appears. It is defined as the ratio between the wavelength and the FWHD:

$$Q = \frac{\lambda}{FWHD} \approx \frac{2\pi n_g L}{\lambda\kappa^2} = \frac{n_g L}{\lambda}\mathcal{F}. \tag{2.33}$$

2.2.1 The NLSE in Ring Resonators

As mentioned earlier, the NLSE derived in section **2.1** can be modified and expanded. By modifying the NLSE to include further constraints it can be used to describe the temporal evolution of the intracavity field in a fiber ring resonator. A general model of the evolution of the intracavity field can be derived using an *infinite-dimensional Ikeda map*. This map is derived by combining the ordinary NLSE in Eqn. (2.13) together with boundary conditions that relates the fields between each round-trip inside fiber cavity. Assuming a slowly-varying field envelope the field at each round-trip m can be described as:

$$E^{(m+1)}(0,\tau) = TE_{in} + RE^{(m)}(L,\tau)e^{i\phi_0}, \tag{2.34}$$

$$\frac{\partial E^{(m)}(z,\tau)}{\partial z} = -\frac{\alpha}{2}E^{(m)}(z,\tau) - \frac{i}{2}\beta\frac{\partial^2}{\partial\tau^2}E^{(m)}(z,\tau) + i\gamma|E^{(m)}(z,\tau)|^2E^{(m)}(z,\tau). \tag{2.35}$$

The term $E^{(m)}(z,\tau)$ describes the intracavity fields during the roundtrip m, z is the longitudinal direction in the resonator and τ is a time (here, within the reference frame moving at the group velocity). L is the length of the resonator, θ describes the power transmission at the coupling point. The parameter ϕ_0 is a linear phase accumulated by the intracavity field during one roundtrip in the resonator with respect to the external pump field.

Low-Loss Structures: Mean-Field Theory

In a structure that exhibits low loss the relative change in the intracavity field over a single round trip is negligible. In this case the external pump field and the coupling loss can be averaged out over the full length of the cavity and the problem can be described using the mean-field theory. This essentially means that Eqn. (2.34) and Eqn. (2.35) can be averaged into a single driven and damped NLSE similar to that of Eqn. (2.13). Following the approach in [14] we start out with the NLSE that we found in 2.13 where we now note that the field is dependent on the round trip number such that:

$$\frac{\partial E_m}{\partial z} = -\frac{i}{2}\beta_2\frac{\partial^2 E_m}{\partial\tau^2} + i\gamma|E_m|^2E_m. \tag{2.36}$$

By performing an integration of Eqn. (2.36) at each round trip following the initial boundary condition provided by the Ikeda map. For the evolution of a pulse envelope travelling inside of a ring resonator the Ikeda map takes the form:

$$E^{(m+1)}(0,\tau) = tE_{in}(\tau) + rE^{(m)}(0,\tau)e^{-i\phi_0}G_L, \quad m = 0,1,2,... \tag{2.37}$$

This equation is very similar to the one presented in Eqn. (2.34). We have the transmission and reflection coefficient t and r where $|t|^2 + |r|^2 = 1$. ϕ_0 is the cavity phase detuning at the pump frequency ω_0 and finally, G_L is an operator that accounts for the nonlinear propagation of the pulse over a round trip in the resonator of length L. The input field $E_{in}(\tau)$ does not depend on the round trip number m. The term $G_LE^{(3)}(0,\tau)$ is determined by the previous round trip. At $m = 0$, the term equals zero. Since we have restricted this analysis to low loss structures the temporal evolution of the intracavity field is considered slow in comparison to the round trip time t_R. Due to this slow evolution of the field inside the cavity we can introduce a new slow time scale t to describe the change in the intracavity field at each round trip at the point $z = 0$. This new slow time scale can replace the round trip number m such that we are able to define:

$$E(t,\tau) = E_m(0,\tau). \tag{2.38}$$

where the slow time t is defined as an integer number of the round trip time, $t = nt_R$. We also introduce the derivative of Eqn. (2.38):

$$t_R \frac{\partial E(t,\tau)}{\partial t} = E_{m+1}(0,\tau) - E_m(0,\tau). \tag{2.39}$$

Both cavity detuning ϕ_0 and the nonlinear phase change $\gamma L|E|^2$ are assumed to be much smaller than one. Furthermore, we assume that the length of the loop is much smaller than the length of the pulses that are formed inside of the resonator. Doing this allows us to average the RHS of Eqn. (2.36) over the resonator length L and thereby obtain:

$$G_L E_m(0,\tau) = -i\frac{\beta_2}{2} L \frac{\partial^2 E_m(0,\tau)}{\partial \tau^2} + i\gamma L |E_m(0,\tau)|^2 E_m(0,\tau). \tag{2.40}$$

If we also consider the initial phase detuning ϕ_0 and the cavity loss α (and neglect all higher order terms):

$$E_{m+1}(0,\tau) = TE_{in}(t) + E_m(0,\tau) - i\phi_0 E_m(0,\tau) - \frac{\alpha}{2} E_m(0,\tau) + i\frac{\beta_2}{2} L \frac{\partial^2 E_m(0,\tau)}{\partial \tau^2} + i\gamma L |E_m(0,\tau)|^2 E_m(0,\tau). \tag{2.41}$$

Introducing the expression from Eqn. (2.38) and Eqn. (2.39) we finally arrive at:

$$t_R \frac{\partial E(t,\tau)}{\partial t} = \underbrace{TE_{in}}_{\substack{\text{Cavity} \\ \text{transmission}}} + \Bigg[\underbrace{-i\frac{\beta_2}{2} L \left(\frac{\partial^2}{\partial \tau^2} \right)}_{\text{GVD}} + \underbrace{i\gamma |E(t,\tau)|^2}_{\substack{\text{Kerr} \\ \text{nonlinearity}}} - \underbrace{i\phi_0}_{\substack{\text{Phase} \\ \text{detuning}}} - \underbrace{\frac{\alpha}{2}}_{\substack{\text{Cavity} \\ \text{losses}}} \Bigg] E(t,\tau). \tag{2.42}$$

Comparing to the NLSE we derived for a straight waveguide, Eqn. (7.38), the two equations are very similar. The NLSE for a microring resonator has the exact same terms as the NLSE for the waveguide but contains two extra terms related to the cavity. Besides the GVD, the Kerr nonlinearity and the cavity loss terms it also includes a cavity transmission term and a term containing the phase detuning that is needed in order to couple in light to the cavity.

2.3 The Si_3N_4 Platform

Dielectric waveguides consist of a core of refractive index n embedded in another dielectric layer called the cladding. The cladding has a lower refractive index which allows for the light to be confined inside of the waveguide due to total internal reflection (TIR).

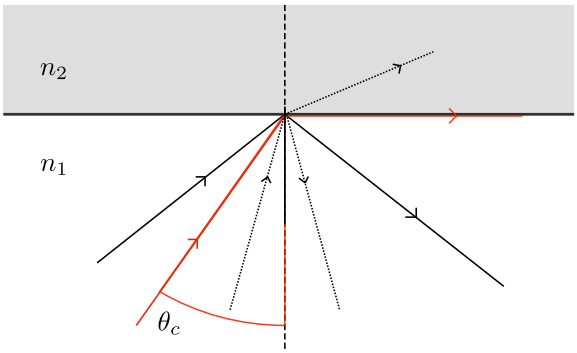

Figure 2.6: Snell's law of refraction. The total internal reflection happens at the critical angle θ_c.

Light travelling from one medium to another may change its direction of propagation when there is a change in the refractive index. The condition for TIR are found from Snell's law which describes the relation between the direction of propagation in two medium:

$$n_1 \sin\theta_1 = n_2 \sin\theta_2, \tag{2.43}$$

where θ_1, θ_2 are the incident and output angles and n_1,n_2 in our case are the refractive indices of the core and the cladding, respectively. TIR can only occur in the case where light is travelling from a high index medium to a lower index one. The critical angle can be found from the relation:

$$\theta_c = \sin^{-1}\left(\frac{n_1}{n_2}\right). \tag{2.44}$$

This means that as long as $\theta_2 > \theta_c$ light will propagate inside the core of the waveguide. An example of Snell's law including the critical angle is illustrated in Figure 2.6.

The extent of the confinement relates to the disparity in refractive index. A larger index contrast between the refractive index of the core and the cladding will lead to a increase in the degree of confinement. The index contrast is mathematically described as:

$$\Delta n = \frac{n_1^2 - n_2^2}{2n_1^2}, \tag{2.45}$$

where n_1 and n_2 are the refractive indices of the core and the cladding, respectively [26].

Chip-based structures are created using a wafer-scale technology and are often referred to as photonic integrated circuits (PICs). The waveguide structures are fabricated onto support substrates (often referred to as the chip). These substrates are typically made of materials like silicon or silica but can also be made of nonlinear crystal materials such as lithium niobate ($LiNbO_3$).

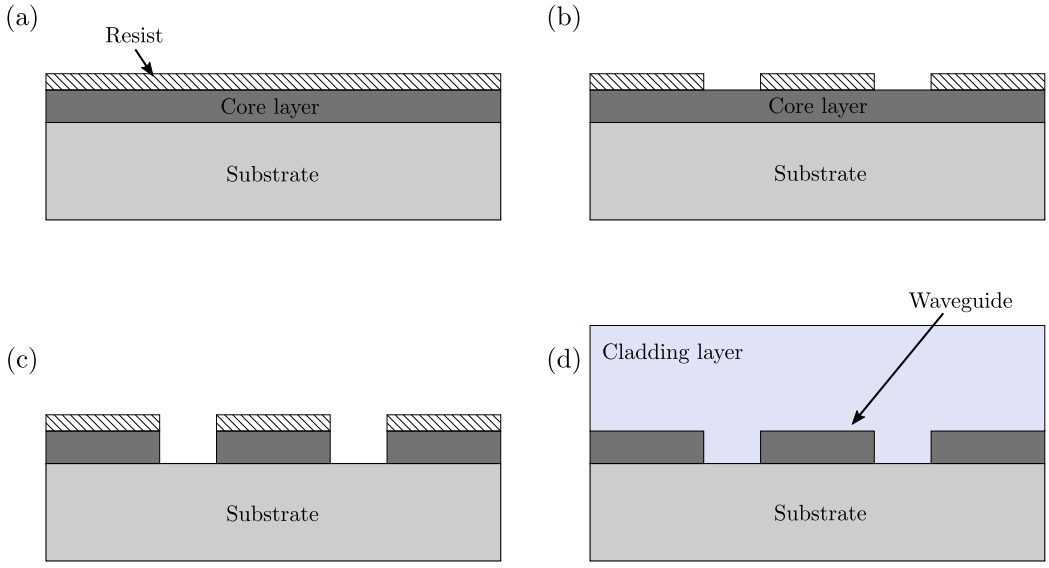

Figure 2.7: Example of process flow chart for a PIC. (a) The raw chip with a core layer on top of a substrate coated with a layer of resist, (b) exposure pattern after being subject to EBL, (c) the pattern from the EBL is transferred to the core layer through an etching process, and (d) the remaining resist is removed and a cladding layer is deposited on top.

The fabrication process can vary depending on the device and there exists several methods that are used for the fabrication of integrated circuits but that is out of the scope of this thesis. A typical (simplified) fabrication process flow using electron beam lithography (EBL) is illustrated in Figure 2.7.

The EBL is a technique that uses a focused electron beam to create a pattern in the top layer, the *resist*), that causes a molecular change in the material changing its solubility. After the EBL exposure, depending on the type of resist which can be positive or negative, the exposed (positive) or the unexposed (negative) will be removed by the developer. This leaves the core layer exposed on which the pattern can be transferred using a technique called etching leaving the waveguide structures behind. The etching is a process in which a layer can be removed from the surface of a wafer/chip. There exist two methods of etching: (1) Dry etching that uses a plasma or vapor to remove the material or (2) wet etching in which liquid chemicals are used.

The chip we have been using in our experiments is designated as Wafer 266-BSS1-I0p5. The device is a Si_3N_4 platform with a diameter of 217 μm provided to us by the Department of Microtechnology and Nanoscience (MC2) at Chalmers University of Technology. Silicon Nitride or Si_3N_4 is a dielectric material with a refractive index of around $n = 2$. The cladding used for this device is LPCVD[3] SiO_2 with a refractive index of around $n = 1.4$. Figure 2.8 shows a similar Si_3N_4

[3]Low pressure chemical vapor

waveguide structure fabricated at Chalmers.

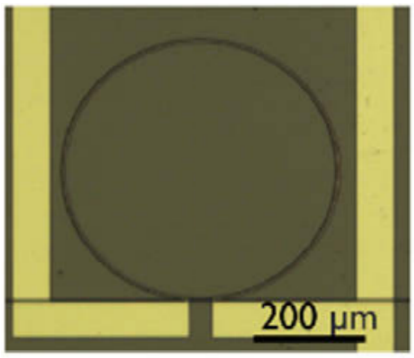

Figure 2.8: An image of a Si_3N_4 waveguide structure designed by Chalmers. The golden bands are integrated heater elements. This structure is similar to the one we have used for our experiments. The figure is adapted from [27].

Chapter 3

Dynamics of Frequency Comb Generation

The focus of this project has been on the generation of frequency combs based on MRRs also known as micro-combs or Kerr frequency combs. One of the advantages of micro-combs is that they are integratable on chip-scale. This means that they can be produced at a low cost on a integrated platform which also makes them a compact solution compared to traditional commercially available frequency combs. Another advantages is the freedom in the design of the dispersion. The geometry of the design can be used for dispersion engineering which means that we are not bound by the material dispersion.

The materials used for the fabrication of MRR typically exhibits strong second or third order nonlinear effects. The choice of material plays a crucial role in frequency comb generation. A comb in an MRR is generated through the nonlinear process of parametric frequency conversion using a continuous wave (CW) laser. In the MRR, light gets trapped and confined which then allows it to acts as a parametric oscillator where pump photons can be converted into signal-idler pairs [10]. This is illustrated in Figure 3.1 for the case known as four wave mixing (FWM).

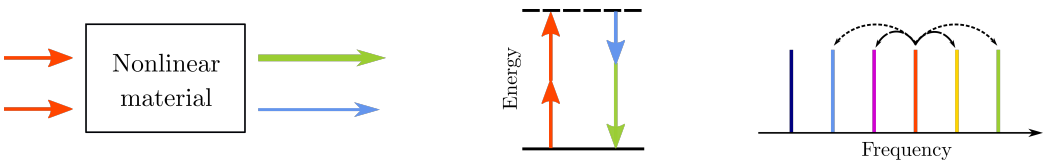

Figure 3.1: Illustration of FWM in a nonlinear material. The red arrows are pump photons and the blue (idler) and green (signal) arrows corresponds to the signal-idler pair.

3.1 Four Wave Mixing

FWM is a third order parametric process that involves nonlinear interaction between four optical waves. The effect occurs when two pump photons annihilates and creates two photons of new frequencies - a so called *signal-idler* pair. The process can be viewed as one photon gaining energy and the other one loosing energy conserving the total energy of system.

The parametric processes are most commonly divided into second-order $\chi^{(2)}$ or third-order $\chi^{(3)}$ processes depending on what order susceptibility is responsible. The nonlinear response of a material is expressed in terms of the induced polarisation which can be expressed in terms of a power series:

$$\mathbf{P} = \epsilon_0\chi^{(1)}\mathbf{E} + \epsilon_0\chi^{(2)}\mathbf{E}^2 + \epsilon_0\chi^{(3)}\mathbf{E}^3, \tag{3.1}$$

where $\mathbf{E}$ is the electric field, ϵ_0 is the vacuum permittivity, and χ^n is the n^{th} order susceptibility which is expressed as a tensor of rank $n+1$. As an example, the third-order nonlinear polarisation is written:

$$\mathbf{P}_{\mathrm{NL}} = \epsilon_0\chi^{(3)}\mathbf{EEE}. \tag{3.2}$$

Isotropic materials such as Si_3N_4 exhibits spatial inversion symmetry which means that all even-ordered contributions in Eqn. (3.1) such as the second-order susceptibility $\chi^{(2)}$ will cancel out of the equation and only the odd-numbered terms will contribute.

FWM can be either degenerate or non-degenerate. In the non-degenerate case the two pump photons are not of the same frequency hence:

$$\omega_{p_1} + \omega_{p_2} = \omega_s + \omega_i, \quad \omega_{p_1} \neq \omega_{p_2}. \tag{3.3}$$

In the degenerate case the two initial photons are of identical frequency and therefore only three frequencies are considered. In order to maintain the conservation of energy it is required that:

$$2\omega_p = \omega_s + \omega_i, \tag{3.4}$$

in which ω_p is the pump frequency and ω_s and ω_i is the signal-idler pair. In a microresonator pumped with a CW laser the initial FWM will be degenerate since the pump only consists of a single frequency: $\omega_1 = \omega_2$.

3.1.1 FWM and Comb Generation

To initiate the generation of sidebands in the MRR the parametric gain must exceed the losses of the cavity. The parametric gain:

$$g = \sqrt{(\gamma P_p)^2 - (\Delta k_{NL}/2)}, \tag{3.5}$$

is dependent on the pump power P_p, the nonlinear coefficient γ, and lastly also a nonlinear phase mismatch Δk_{NL} between the propagation constants of the signal, idler and pump waves. The phase mismatch is due to chromatic dispersion $k = n\omega/c$, resulting in waves propagating at different wavelengths experiencing different refractive indices. It leads to a shift of the resonator modes causing a change of the spacing between the resonator modes with respect to the optical frequency. In order to achieve cascaded FWM at a level at which a comb can be generated the phase mismatch has to approach zero. For this to be true the phase-matching condition must be fulfilled.

However, due to a combination of self- (SPM) and cross-phase modulation (XPM) from the Kerr effect arising at higher intensities there will be a nonlinear phase-mismatch between the wave vectors:

$$\Delta k_{NL} = k_s + k_i - 2k_p + 2\gamma P_p, \tag{3.6}$$

where k_s, k_i, and k_p are the signal, idler and pump waves, respectively [1]. The nonlinear coefficient γ is related to the properties of the waveguide:

$$\gamma = \frac{n_2 \omega_p}{c n A_{eff}}, \tag{3.7}$$

with A_{eff} being the effective mode area and n_2 the nonlinear refractive index. For a given polarisation n_2 can be related to the third order nonlinearities through $n_2 = \frac{3}{8}\chi^{(3)}_{eff}$, where $\chi^{(3)}_{eff}$ is the effective third order susceptibility.

The last term in Eqn. (3.6) can never assume negative values. This means that in order to fulfill the phase-matching condition the sum of $k_s + k_i - 2k_p$ have to have a negative value.

As stated earlier, the refractive index n is frequency dependent and this will lead to a shift of the resonator modes resulting in a change of the spacing between the resonator modes with respect to the optical frequency. This effect is divided into two regimes: the normal and anomalous dispersion regime. In the normal dispersion regime the modes will moves closer together as the mode frequency increases leading to $k_s + k_i - 2k_p > 0$. Whereas, in the anomalous dispersion regime the mode spacing will increase as the mode frequency increases, $k_s + k_i - 2k_p < 0$. It then becomes obvious that only in the anomalous dispersion regime can we obtain a zero-phase mismatch.

3.1.2 FWM in MRRs

The MRR entails some constraints regarding the cavity modes. For the wave vectors it leads to the resonance condition:

$$k = \frac{2\pi m}{L} \quad \text{with} \quad m = 1, 2, ..., \tag{3.8}$$

where m is the cavity mode number and L the effective length of the MRR. Based on the work presented in [1] by Agha et. al done, if the signal-idler pair are

assumed to be symmetrically placed around the pump at a distance of $\pm n$ orders away, according to their mode number m, then $\Delta k = 0$ on resonance. Assuming a strong pump the cavity modes can be expressed as:

$$\omega_p = \frac{2\pi mc}{(n_{\text{eff}} + n_2 I_p)L}, \tag{3.9}$$

and

$$\omega_{i,s} = \frac{2\pi(m \pm n)c}{(n_{\text{eff}} + 2n_2 I_p)L}, \tag{3.10}$$

where I_p is the intensity of the intracavity pump, n_{eff} is the effective refractive index, and n_2 is the nonlinear refractive index. To satisfy the energy preservation and the phase-matching condition:

$$\omega_p = \omega_s + n\Delta\omega = \omega_i - n\Delta\omega, \tag{3.11}$$

with $n\Delta\omega$ corresponding the pump and the signal-idler being on resonance with cavity modes with the consideration of refractive index of the cavity modes.

3.2 Group Velocity Dispersion

The nonlinear effects necessary in the generation of a MRR based frequency comb strongly depends on the group velocity dispersion (GVD). The group velocity is what characterises the velocity at which a pulse propagates through a medium. If that said medium is made up of a material that exhibits dispersion, then the group velocity will be dependent on the wavelength and that dependency is known as the GVD.

As with the chromatic dispersion, the GVD can be either normal or anomalous depending on the sign of the parameter and that will affects the pulse by pulse compression, either creating positive or negative chirp, respectively. Normal dispersion refers to the case in which the group velocity decreases when the optical frequency increases causing lower frequency components to travel faster than high frequency components and vice versa for anomalous dispersion [18].

The dispersion in a MRR can be described through the Taylor expansion series around $\mu = 0$:

$$\omega_\mu = \omega_0 + D_1\mu + \frac{1}{2}D_2\mu^2 + \frac{1}{6}D_3\mu^3 + ..., \tag{3.12}$$

where ω_μ is the resonance frequency with a given mode number μ with respect to the pump laser (denoted $\mu = 0$). The parameter D_1 is the first order dispersion describing the free spectral range (FSR) of the resonator, D_2 is the second order dispersion related to the GVD, and lastly D_3 is the third order dispersion. The second order dispersion D_2 is related to the the GVD through the relation:

$$D_2 = -\frac{c}{n}D_1^2\beta_2. \tag{3.13}$$

A positive D_2 indicates anomalous dispersion with $\beta_2 < 0$. The majority of generated combs are achieved in a regime where the MRR exhibits anomalous dispersion ($\beta_2 < 0$).

Chapter 4

Dispersion Measurements

The dispersion of the MRR device can be determined by measuring the spectral distance between adjacent resonator modes over a wide area ($\sim$ 100 nm). The more linear the scan is the better and the more precise the measurement is going to be since there will be no variation in distance between data points. A linear scan is characterised by having a constant scan speed throughout the full measurement. However, this is rarely the case. Most lasers will vary somewhat in scan speed over a distance which means that they typically will start to accelerate and then slow down again repeatedly over the full distance. Therefore, it is necessary to come up with another way of linearising the scan. Typically, this is done by calibrating the laser scan to a reference cavity. An ideal cavity has perfectly equidistantly spaced resonances. In theory this should mean that the more points provided by the reference source the more precisely the laser scan can be calibrated. If, however, the cavity is subject to dispersion the cavity resonances will no longer be evenly spaced.

The most commonly used source of reference is a fibre interferometer due to the wide availability and compact size. Like with any other type of interferometer, the fringe spacing of a fibre interferometer can be adjusted depending on the length of the interferometer making it possible to create an arbitrary amount of reference points. The disadvantage of this method of reference, however, is that the fibre will be subject to dispersion which will affect the measurements. Nevertheless, the effect can be accounted for by either adding another reference to the setup or by characterising the interferometer beforehand.

For our dispersion measurements conducted on the SiN resonator we decided to build a free space cavity to use as reference. The free space cavity makes it possible to create a relatively dispersion-free reference compared to a typical fibre interferometer. Comparing the two, the change in refractive index from 1530 nm to 1630 nm for air is on the order of $\Delta n = 1 \cdot 10^{-7}$. A typical fibre made from fused silica (SiO_2) is on the order of $\Delta n = 1 \cdot 10^{-3}$. The change in effective refractive index of the MRR is around $\Delta n = 3 \cdot 10^{-3}$ [1] making it significantly larger than

[1] Calculated for a Si_3N_4 layer of thickness 750 nm.

that of the free space cavity [13] [20].

The cavity consists of two concave high-reflectance mirrors placed at each end of a 1480 mm long aluminum profile. The mirrors have a radius of curvature (ROC) of 2 metres and a reflectance of 99.7 %. This results in a FSR of 101.3 MHz which should provide roughly 10^3 reference points between the adjacent resonator modes of the MRR.

A schematic overview of the setup can be seen in Figure 4.1. A continuously tunable laser from Toptica (Toptica DLC pro) is used to scan the wavelength from 1520 nm to 1630 nm. The laser uses a frequency selective grating element to control the frequency of the output emission. The grating is designed to reflect the first order diffraction back into the laser diode as feedback while the zeroth-order diffraction is reflected as the output [25] [7]. The lasing frequency depends on the angle between the beam coming from the laser diode and the grating (commonly referred to as the Littrow angle). So, by changing the angle the lasing frequency can be changed. A typical Littrow ECDL configuration is shown in Figure 4.2.

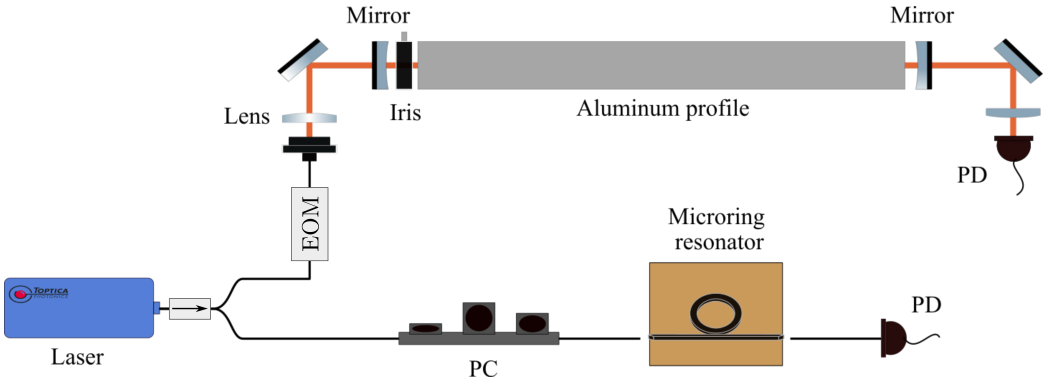

Figure 4.1: Schematic overview of the dispersion setup. The laser output is divided into two using a 3 dB coupler. One path goes through the MRR and the other goes through a free space cavity. The free space cavity is used as a reference to calibrate the frequency axis of the MRR transmission data. EOM: Electro-optical modulator, PC: Polarisation controller, PD: Photo detector.

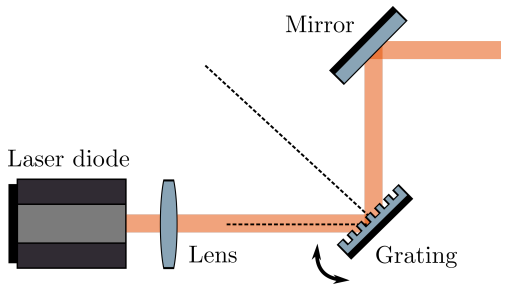

Figure 4.2: A typical Littrow ECDL configuration. The angle of the grating is used to change the lasing frequency.

The output of the laser is split in two using a 3 dB fibre coupler. One part of the light is sent through the MRR and the other part goes through the free space reference cavity. The light going to the free space cavity is first sent through a fibre EOM. The EOM is only used to measure the FSR of the free space cavity after which it is removed. The light is then coupled into free space and the output beam is collimated using a plano-convex lens. The cavity transmission signal is detected by a photo detector (PD) and recorded on an oscilloscope. The second part is sent through a polarisation controller (PC) and coupled into the MRR using tapered lensed fibres [2]. The tapered fibres couples the light into the bus waveguide of the MRR. The transmission signal from the MRR is detected on another photo detector and recorded on the same oscilloscope as the free space cavity transmission signal.

The transmission signals of the free space cavity and the MRR are shown in Figures **??** and 4.3. The FSR of the free space cavity is measured using the EOM to be 96.9 MHz. The transmission of the MRR approaches zero on the resonance which shows a good coupling between the bus waveguide and the MRR.

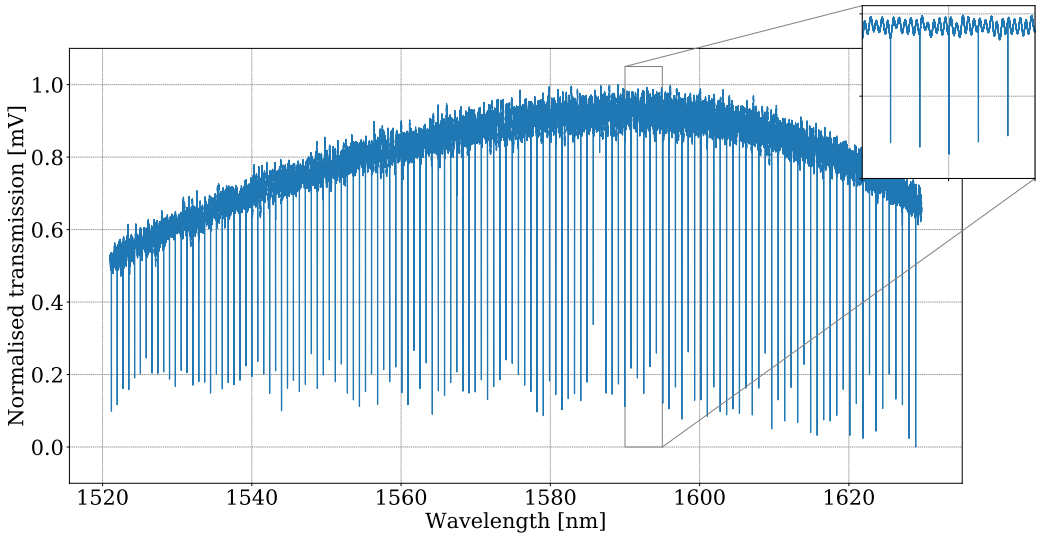

Figure 4.3: Transmission spectrum of the Wafer 266-BSS1-I0p5-R227 from 1520 nm to 1630 nm plotted against the calibrated axis.

Calibration of the Laser Scan

In order to calibrate from a scan speed to a linear frequency axis we use the transmission peaks of the free space cavity. We assume the cavity to be dispersion-free which means that every distance between two neighbouring resonances must equal one FSR of 96.9 MHz.

[2]The fibres have a focal length of 14 μm and a 2.5 μm spot size.

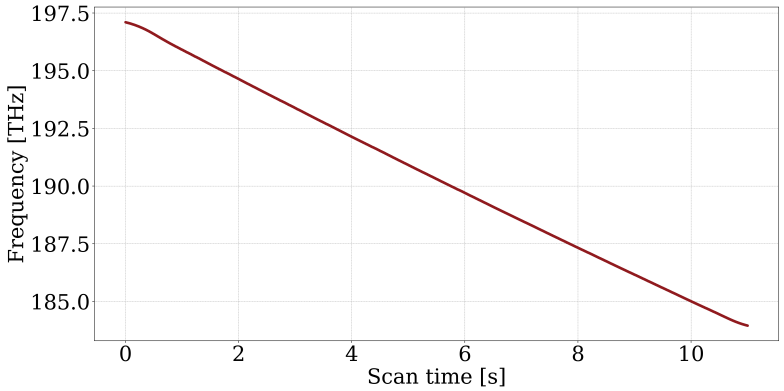

Figure 4.4: Scan time in seconds plotted against the calibrated frequency axis.

First of, we locate every resonance peak in the data set between two points in time marking the start and the end of the scan. The peak values in time are then gathered in an array and the first index is set to 0 Hz. From here, the number of points between to adjacent indices are equally distributed such that the total distance between each peak equals 96.9 MHz. The result is a new array of length $(n-1) \cdot 96.9$ MHz, with n being the number of peaks. This array constitutes the calibrated array in which we assume the scan speed to be linear between each resonance peak.

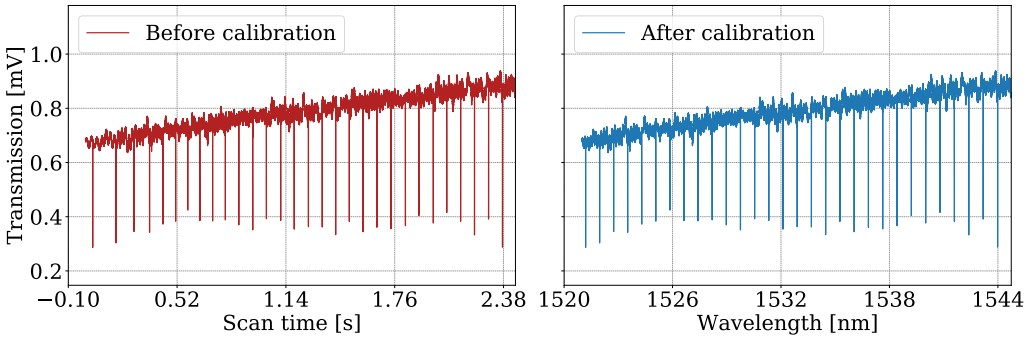

Figure 4.5: Comparison of the un-calibrated vs. the calibrated laser scan. (**Left**): un-calibrated, (**right**): calibrated.

When comparing the raw time axis with the calibrated frequency axis, the change in scan speed of the laser is most visible in the beginning and the end of the scan as it is possible to see from figure 4.4. A comparison of the un-calibrated vs. the calibrated scan in the beginning of the scan is shown in Figure 4.5. Here the same tendency seen in Figure 4.4 is observed. We see how the distance between transmission peaks varies in the un-calibrated scan whereas in calibrated scan they are evenly spaced.

4.1 Characterisation of the MRR

Once the laser scan has been calibrated the MRR can be characterised by looking at the quality factor Q and dispersion of that device. To find the Q-values, each of the MRR resonances are fitted to a Lorentzian function:

$$T(x) = A \cdot \frac{1}{1 + \left[\frac{(x_0 - x)}{\gamma/2}\right]^2} + B, \tag{4.1}$$

where A is the amplitude, B is an offset, x_0 is the frequency of the peak, and γ is the width at FWHM.

The Q-value is obtained by dividing the peak position x_0 with the width γ of the resonance acquired from the fit. The calculated Q-value we obtain from the fit is the total transmitted Q-value, Q_t. Q_t (or alternatively Q_{tot} or Q_{loaded}) is a measure of the combined system including the losses. It is not a complete measure of the quality of the MRR device. This means that it does not distinguish, in this case, between material (intrinsic) losses Q_i and coupling losses Q_c related to the coupling between the bus waveguide and the MRR.

Typically, the intrinsic Q is noticeably larger than Q_t because it takes all losses into account - both material and coupling losses - and are able to distinguish between them. At low powers Q_c can be found by the expression [3]:

$$Q_c = \frac{2Q_t}{(1 + \sqrt{T_{min}})}, \tag{4.2}$$

where $T_{\min}$ is the the minimum of the normalised transmission, i.e. the peak value of the transmission peak. The Q of most interest when characterising the MRR is the intrinsic Q, Q_i and once Q_c is known, Q_i is easily found through the relation:

$$\frac{1}{Q_t} = \frac{1}{Q_c} + \frac{1}{Q_i}. \tag{4.3}$$

The results obtained from our fitting routine of the MRR resonances are shown in Figure 4.6.

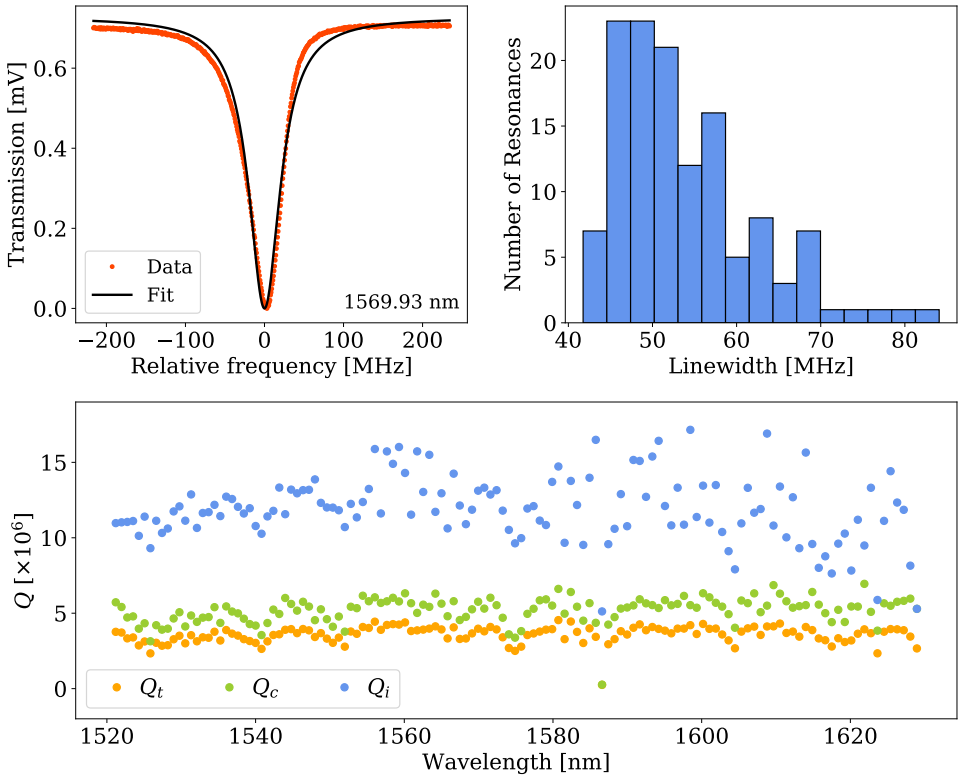

Figure 4.6: Characteristic of Q_{tot} of Wafer 266-BSS1-I0p5. (a) A representative resonance with a FWHM of 47.70 MHz. (b) Histogram of the obtained linewidths from the MRR. (c) Q_{tot} calculated from the parameters estimated by the Lorentzian fit shown in (a).

Figure 4.6(a) shows a single MRR resonance with a linewidth of $\gamma = 48.06$ MHz and a peak value $x_0 = 1569.93$ nm. To show the distribution of the resonance linewidths a histogram of all the obtained linewidths are plotted in Figure 4.6(b). The Q_{tot} is plotted as a function of wavelength in Figure 4.6(c). The outlier at 1586.5 nm is due to a strong mode crossing in the device. Sometimes higher order modes can exist in the resonator and if so they will interact with the fundamental mode which will lead to avoided mode crossings.

To characterise the dispersion of the device the D_1, D_2, and D_3 are estimated from fitting the variation in frequency to Eqn. (3.12):

$$\omega_\mu = \omega_0 + D_1\mu + \frac{1}{2}D_2\mu^2 + \frac{1}{6}D_3\mu^3 + ...,$$

where β_2 is found from the relation in Eqn. (3.13):

$$D_2 = -\frac{c}{n}D_1^2\beta_2.$$

The dispersion of the device is highly dominated by the FSR so in order to form

an idea of the behaviour of the higher order dispersion the dispersion profile is plotted as a function of the integrated dispersion in Figure 4.7. The integrated dispersion is often a useful measure when describing the dispersion since it is used to describe how much a given resonance deviates from a grid in which the spacing between each resonance is equidistant [11]:

$$D_{\text{int}}(\mu) = \omega_\mu - (\omega_0 - D_1\mu). \tag{4.4}$$

The belonging residuals in Figure 4.8. We obtain a relatively high value for the standard deviation of the residuals compared to when we look at the fit in Figure 4.7. This is due to the outliers which stems from mode crossings. The values found from the fit are $D_1/2\pi \approx 100.2882$ GHz, $D_2/2\pi \approx 0.619$ MHz, and $D_3/2\pi \approx -0.0003$ MHz. Compared to the two other values the effect of $D_3/2\pi$ is negligible. The converted β_2-value is found from Eqn. (3.13). At 1570 nm the refractive index for Si_3N_4 is 1.9957 according to [20] which leads to $\beta_2 \approx -65.2$ ps^2/km.

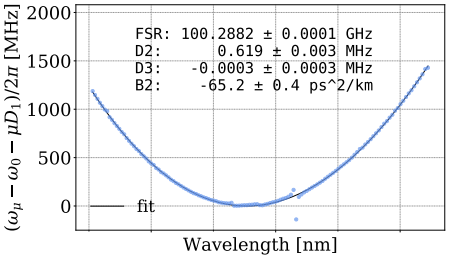

Figure 4.7: Dispersion characterisation of the MRR. Six avoided mode crossings can be seen.

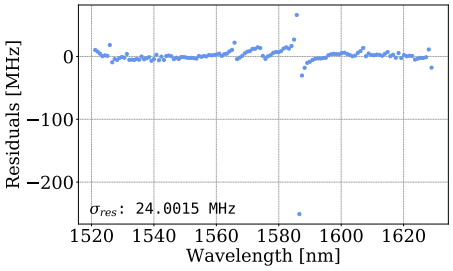

Figure 4.8: Plot of the residuals of the dispersion curve from Figure 4.7.

Six avoided mode crossings can be observed at 1526 nm, 1566 nm, 1574 nm, 1586 nm, 1607 nm, and 1628 nm of which the one at 1586 nm is the most prominent. The rest of the mode crossings are considered fairly weak. The feature stemming from the mode crossings becomes even clearer when looking at the residuals of the four methods in Figure 4.7. The reason why mode crossings are of interest is that they can have an effect on the creation of a soliton comb if the comb is pumped at a wavelength that is too close to a strong mode crossing. At a point of mode crossing the frequencies (and also the decay rate) will change and that shift in frequency will affect the phase matching condition for FWM [19].

4.2 Characterisation of MRR using Higher Order Modes

By adjusting an iris inside of the free space cavity we are able to control how many modes should be excited inside the free space cavity. This gives us the possibility of increasing the number of reference points further by allowing higher

order transverse modes (HOMs) to exist without having to increase the length of the cavity. The use of the HOMs would lead to a finer calibration which could be quite useful in the determination of the Q-value, since it is especially sensitive the local nonlinearities of the laser scan speed. In order to identify the different modes the iris is tightly closed such that the only mode allowed in the cavity is the TEM_{00}. This mode is the easiest to identify due to the shape of its spatial mode profile. It has a Gaussian beam profile with the highest intensity at the center which means that by closing the iris all other modes can be eliminated. From this point the iris is then slowly opened up allowing HOMs to be excited. The TEM_{00} and the HOMs can be seen in Figure 4.9.

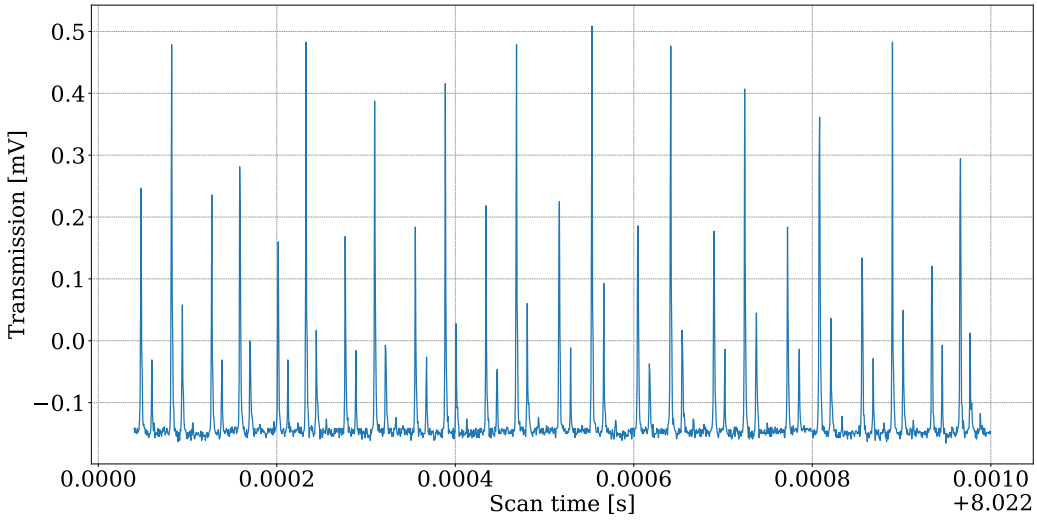

Figure 4.9: Segment of the full transmission signal of the free space reference cavity. The tallest of the modes are the TEM_{00} and the rest are various higher order modes (in this thesis referred to as 1st, 2nd, and 3rd order).

The light entering the free space cavity through the input mirror will travel around inside the cavity. In this time it will be subject to constructive or destructive interference. Constructive interference will occur when the resonator length L is equal to an integer multiple of half the wavelength such that:

$$L = q\frac{\lambda}{2}, \quad q = 1, 2, 3, ... \tag{4.5}$$

Wavelengths that does not meet this condition cannot be supported by the cavity and as a result they will destructively interfere. The frequencies that are supported in the cavity can be found from the expression [24]:

$$\nu_{qmn} = \frac{c}{2L}\left[q + \frac{1}{\pi}(m + n + 1)cos^{-1}\sqrt{g_1 g_2}\right], \tag{4.6}$$

where:

$$g_1 g_2 = \left(1 - \frac{L}{R_1}\right)\left(1 - \frac{L}{R_2}\right), \tag{4.7}$$

where $R_{1,2}$ represent the ROCs of the two cavity mirrors. In the case of equal mirrors the expression becomes:

$$g_1 g_2 = \left(1 - \frac{L}{R_{1,2}}\right)^2. \tag{4.8}$$

The parameter q is associated with the longitudinal mode and describes the node pattern created by constructive interference along the length of the cavity. The integer numbers n and m specify the transverse mode order, i.e. the mode field shape transverse to the propagation direction. The fundamental mode is given by $n, m = 0$. Higher order modes are characterised by having $n, m > 0$ or at least one of the two > 0. For concave mirrors like the ones used in this setup $R_{1,2} > 0$.

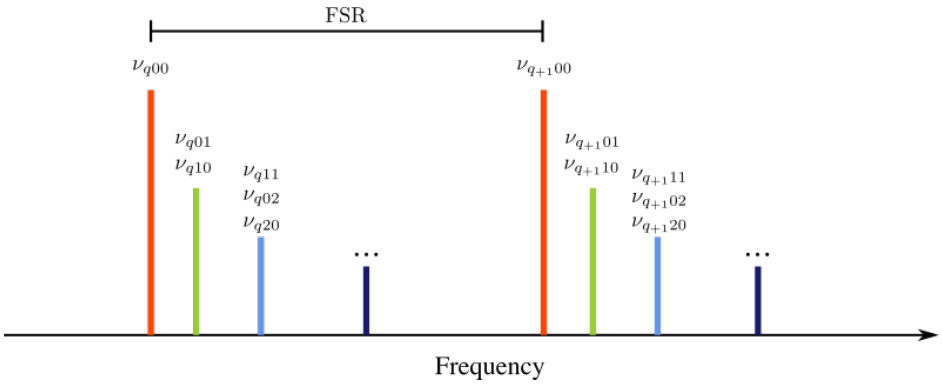

Figure 4.10: Illustration of resonance frequencies in a cavity showing the longitudinal and transverse modes. The distance between two peaks in the same mode family is always equal one FSR.

For the purpose of this setup there is no distinction between the configurations $n, m = 0, 1$, $n, m = 1, 0$, etc. since they will result in the same resonance frequencies found from Eqn. (4.6). The different modes are illustrated in Figure 4.10. Depending on the length of the cavity it is possible for the HOMs for $q = 1$ to be placed more than a FSR away from the ν_{q+100} mode although the distance between two resonances of the same mode family is always one FSR, ex.:

$$\nu_{FSR} = \nu_{q00} - \nu_{q+100} = \frac{c}{2L}. \tag{4.9}$$

To find the distance from the fundamental mode to the different HOMs, we take:

$$\nu_{q00 \to qmn} = FSR - \nu_{q+100} + \nu_{qmn}, \tag{4.10}$$

which gives the relative shift in frequency compared to the fundamental mode with the same q. The theoretical and measured values of the different mode configurations are shown in Table 4.1. The theoretical values are calculated using the measured FSR of 96.9 MHz. The distance between the different mode families are measured using a fibre EOM.

qmn		**100**	**110**	**111**	**121**
$\lvert\nu_{q00\to qmn}\rvert$	Theoretical [MHz]	0.0	56.7	16.5	23.7
	Measured [MHz]	0.0	56.1	15.0	26.0

Table 4.1: The theoretical and measured distances from the fundamental mode to a HOM with configuration qmn. The first column with $qmn = 100$ corresponds to the fundamental mode. For $m + n > 1$ the configuration is subordinate but the sum must corresponds to $m + n = 1, 2, 3, ...$, respectively.

The distance from the fundamental mode TEM_{00} to the HOMs are measured using the sidebands generated on each side of the fundamental mode by the EOM. By tuning the frequency of the sidebands such that they overlap with the resonance of one of the HOMs, the distance in frequency between the two modes can be measured. For simplicity the modes are referred to as: 0th, 1st, 2nd, and 3rd order in this thesis (the 0th order mode being the TEM_{00} mode) because we are not able to distinguish between the different m, n configurations. The reason for this is that we do not have any knowledge on their spatial distribution and therefore we are unable to tell them apart since they will overlap when looking at the transverse modes. Therefore, we are limited to the knowledge regarding the sum of $m + n$. The transmission of the free space cavity showing the distinct excited cavity modes can be seen in Figure (4.11). Note that the transmission here is plotted against time so the image is mirrored compared to Figure 4.10.

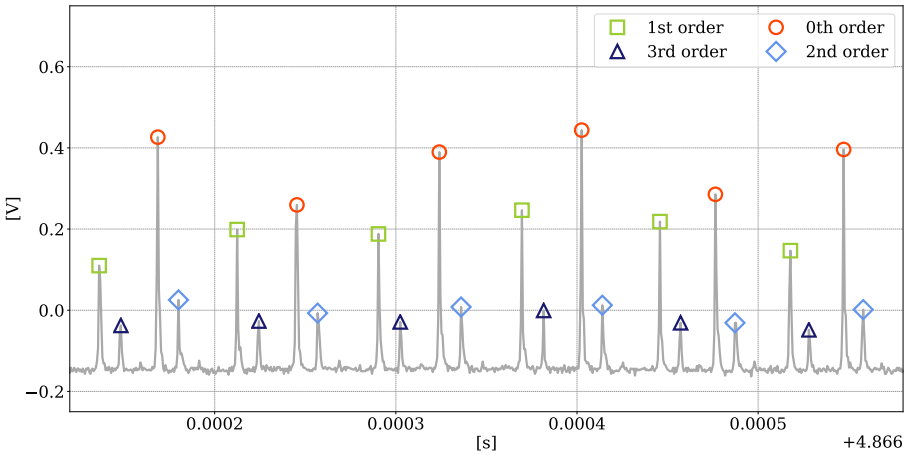

Figure 4.11: Transmission signal for a scan of the input laser frequency showing the HOMs. The distances between the modes are measured to be: 0-3: 26.0 MHz, 3-1: 14.8 MHz, 1-2: 41 MHz, 2-0: 15.0 MHz.

We wanted to to investigate if there was any further improvements or further information to gain by including HOMs in our dispersion analysis compared to only using the 0th order. Using the same data set, we did this by characterising the MRR using four different mode configurations of the free space cavity in order

to calibrate the laser scan. The four different configurations are:

1. All HOMs (0th, 1st, 2nd, and 3rd order),
2. 0th, 1st, and 2nd order,
3. 0th and 1st order,
4. 0th order.

The resulting dispersion curves and fit parameters can be found in Figure 4.12 (a)-(d). Figure 4.12 (e) shows the dispersion curves plotted on top of each other, and in (f) the residuals for the four different methods are shown. The values found from the fits are $D_1/2\pi \approx 100.2882$ GHz, $D_2/2\pi \approx 0.619$ MHz, and $D_3/2\pi \approx -0.0003$ MHz which is similar to the values we got from using only the 0th order mode. The converted β_2-value at 1570 nm is $\beta_2 \approx -65.2$ ps^2/km for all four configurations.

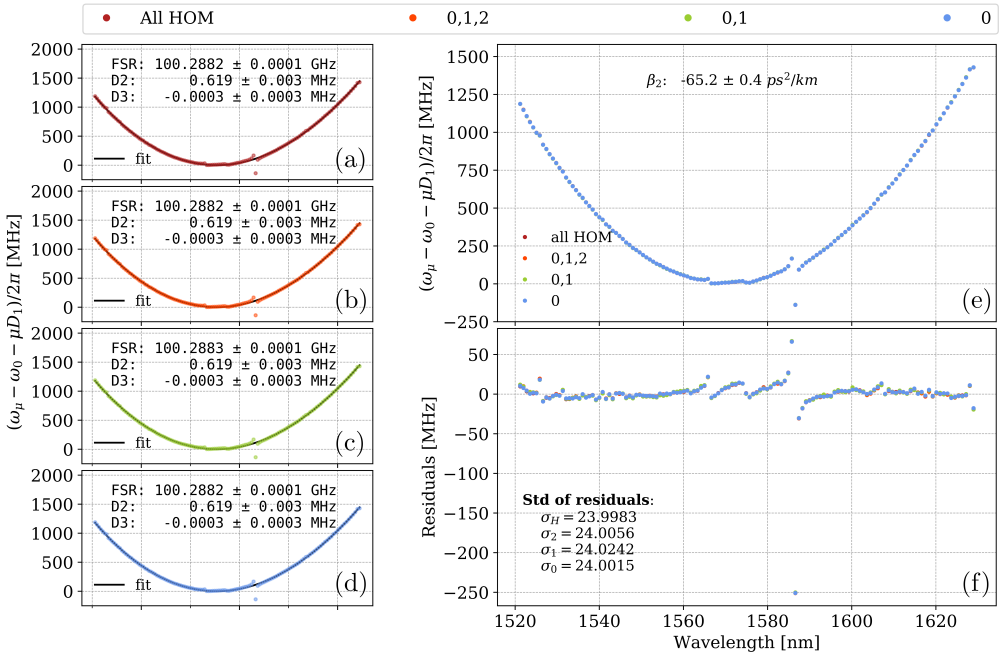

Figure 4.12: Dispersion characterisation of Wafer 266-BSS1-I0p5. (a)-(d) shows the dispersion obtained from each of four methods (all HOMs, only 0th, 0th and 1st, and 0th, 1st and 2nd.). A total of six avoided mode crossing can be observed. In (e) all the dispersion curves are and top of each other and (f) shows the residuals of the four curves from (e). The β_2 value are the same for all four methods.

In order to check the reproducibility of our results we took a total of five measurements. Figure 4.13 shows the standard deviation of the residuals obtained for the four different methods for each of the five data sets. It appears that the measurement itself has a larger influence than the method does. Nonetheless, the

GVD parameter β_2 is within the same uncertainty for all five measurements. In most cases $\beta_2 = -65.2 \pm 0.4$ ps^2/km but in a few of the scans $\beta_2 = -65.3 \pm 0.4$ ps^2/km for some of the methods. In both cases the uncertainty in β_2 was highly dominated by the uncertainty of D_2 - representing the curvature of the dispersion. The uncertainty on D_2 is on the order of seven magnitudes larger than that of D_1. In theory, we should be able to decrease the uncertainty on D_2 by scanning over a larger area which should be easy given that the free space cavity used for reference can be considered dispersion free over the entire range.

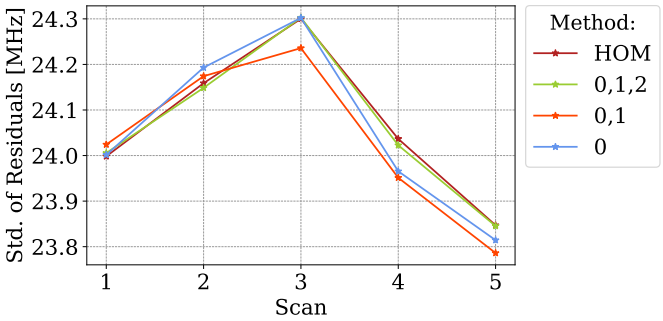

Figure 4.13: Standard deviation of residuals for five different measurements shown for the four methods.

4.3 Linearity of the Laser Scan

From the results presented in Figures 4.6-4.13 it appears that the choice of calibration method does not affect the final results. Without the higher order modes, as mentioned earlier, the number of cavity reference points between two adjacent MRR resonances are roughly 10^3. This implies that the reference cavity does not necessarily have to be as long as it currently is in this setup. A shorter reference cavity would be preferable for more than one reason. Not only would it increase the mobility of the cavity such that it would be easier to move around but it would also make it much easier to align. By artificially removing cavity reference points in our data set we can investigate if a limit exist for which we can no longer assume the laser scan to be linear. If such a limit can be identified it will provide good estimate for how short the reference cavity can be built.

N	1	2	3	4	5	6	7	8	9	10	11	12
Cavity length [cm] :	154.7	77.3	51.6	38.7	30.9	25.8	22.1	19.3	17.2	15.5	14.1	12.9

Table 4.2: Estimated cavity length for each N^{th} 0th order mode removed

Taking every N^{th} ($N = 1, 2, ..., 12$) 0th mode makes it possible to replicate a situation in which we have a cavity of higher FSR. Knowing the FSR we can use Eqn. (4.9) to estimate the length of the reference cavity based on the measured

values. Table 4.2[3] shows the estimated cavity lengths for each N. Figure 4.14 shows the dispersion curve and residuals for $N = 1, 3, 6, 12$.

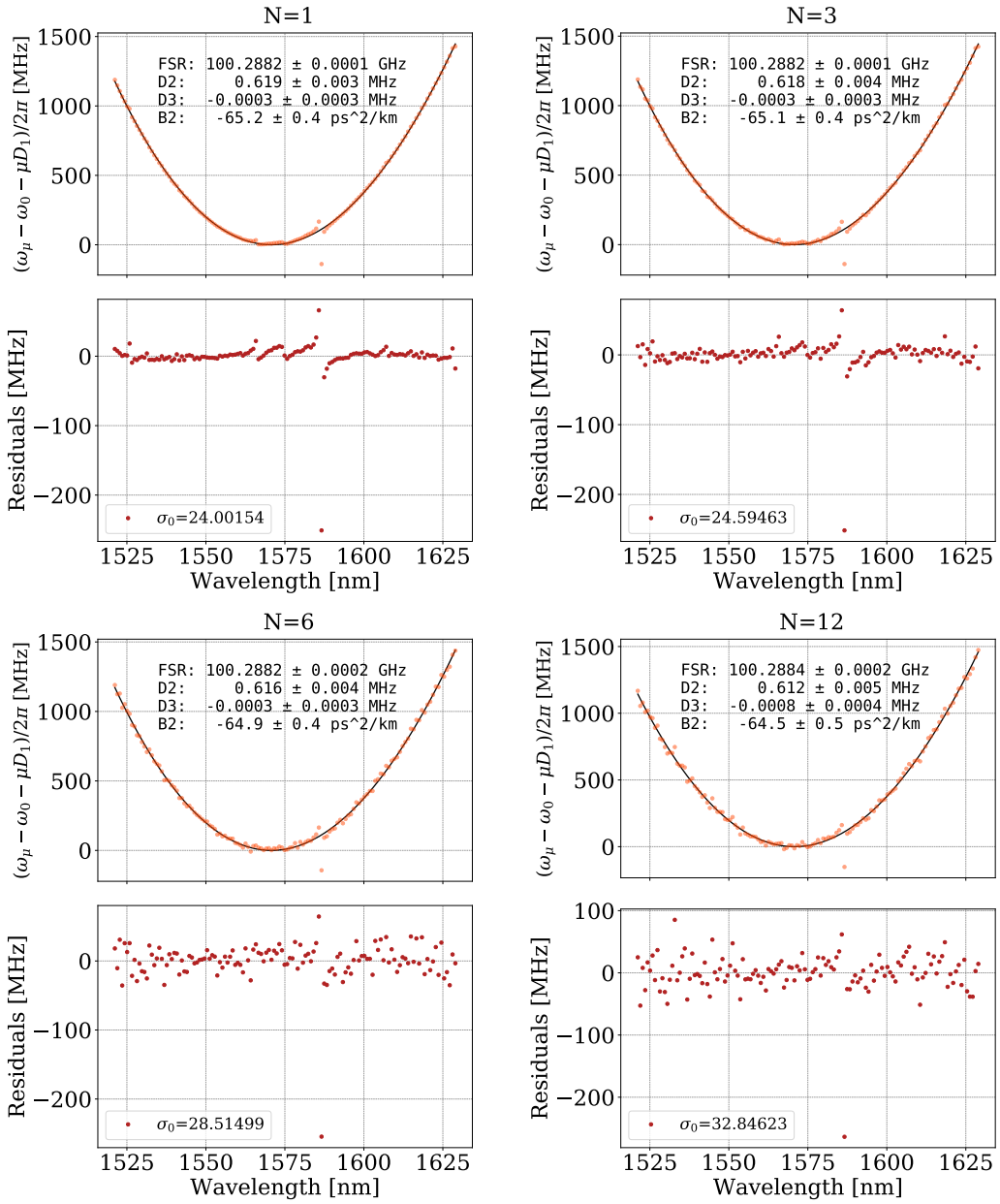

Figure 4.14: Dispersion curves and residuals for every $N^{th} = 1, 3, 6, 12$ 0th order mode removed. The corresponding cavity lengths are 154.7 cm, 51.6 cm, 25.8, 12.9 cm, respectively.

[3]A table containing all fit parameters can be found in Appendix B.

As N is increased and more points are removed the uncertainties of the values obtained from the fit increases as well. Even though the uncertainties increase the values from $N = 3$ and $N = 6$ are both still within the uncertainty of $N = 1$. On the other hand, as N is increased it quickly becomes difficult to identify the weaker mode crossings at 1526 nm, 1566 nm, 1574 nm, 1607 nm, and 1628 nm. This is not an issue when characterising the dispersion of the device but it could pose a problem when measuring the Q-value or if the device is pump near a strong mode crossing when using it for comb generation. As mentioned earlier, pumping the comb close to a mode crossing is not desirable since we want to avoid the shift in frequency.

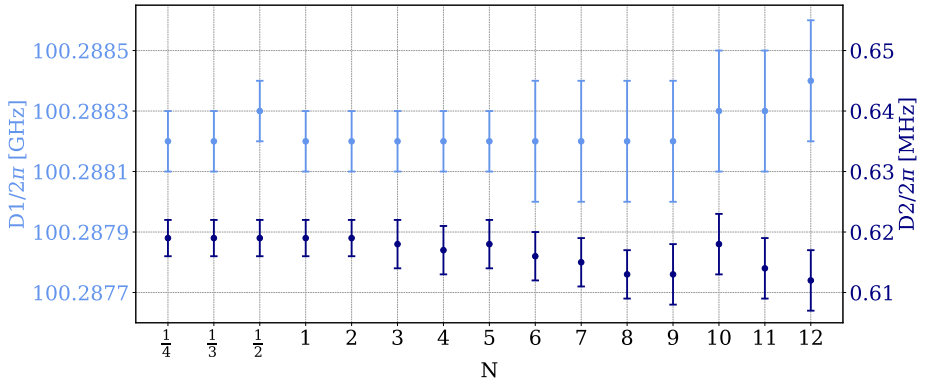

Figure 4.15: FSR (light blue) and D_2 (dark blue) as a function of N shown with errors.

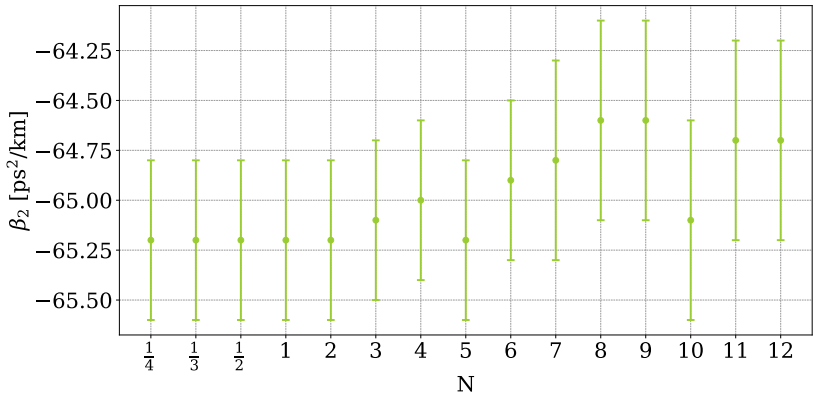

Figure 4.16: β_2 as a function of N shown with errors.

Figure 4.15 shows the FSR and D_2 as a function of N and Figure 4.16 shows β_2 as a function of N. From these two figures we see that even though we only use every 12^{th} 0th order mode we still cannot identify a point were the linearity of the laser breaks. This concludes that a shorter cavity can be a possible replacement compared to the longer one that is present in the current setup. Even though some information regarding the weaker mode crossings are lost, there there is still the

possibility to use the HOMs as additional calibration markers if a higher resolution should be desired, e.g. for better identification of the weaker mode crossings that are not visible otherwise.

Chapter 5

Generation of Frequency Combs

Frequency combs generated in MRRs, also known as microcombs, are typically referred to as Kerr *soliton* combs. Fundamentally, a soliton is a pulse envelope of coherent light that does not change in shape as it propagates through a dispersive medium. They can be described as steady state solutions to the NLSE described in section **2.2.1**. Solitons occur in the MRR as a results of a double balance between the dispersion and the nonlinearities described in Chapter 2 combined with the FWM and cavity losses [11] [9]. In systems where parametric gain is present, such as a microresonator, solitons known as optical dissipative Kerr solitons (DKS), sometimes called bright solitons, can occur. These solitons provide the opportunity to generate broadband coherent frequency combs consisting of ultra-short mode-locked pulse trains [16].

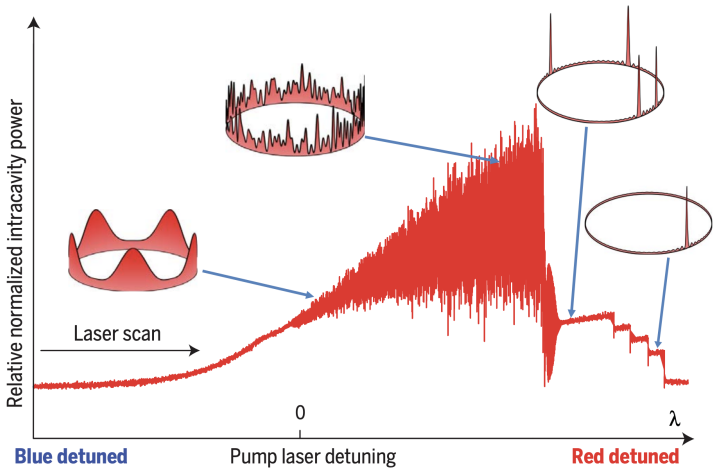

Figure 5.1: An example of a soliton trace signal where the different intracavity soliton configuration are shown. Here the configurations corresponds to (from left to right) (1) formation of primary comb lines, (2) modulation instability (MI), (3) multi-soliton state, and lastly (4) a single soliton state. The figure is adapted from [11].

5.1 Soliton formation in MRRs

The formation of stable solitons can be observed in the trace signal as a series of discrete steps, where each step is correlated to the solitons travelling inside of the cavity. Taking a step down corresponds to the annihilation of individual solitons and at the last step the single soliton step is reached.

The formation of solitons only occurs at the red-detuned side of the MRR cavity resonance where the intracavity field is in a bi-stable regime (i.e. the case where two steady state solutions exists for NLSE presented in section **2.2.1**)[15]. Tuning the laser frequency from the blue-detuned side of the resonance towards the red-detuned side will result in (1) generation of primary combs which then in turn will generate subcomb formation, (2) chaotic MI state, and lastly (3) formation of stable DKS. The formation of stable solitons is observed in the trace signal of the converted intracavity power as a series of discrete steps as illustrated in Figure 5.1. Each step is tied to solitons inside the cavity and a step down corresponds to the annihilation of individual solitons. At the last step a single soliton state is reached which means that only a single soliton exists inside the MRR.

5.1.1 Dissipative Soliton States

A specific soliton state is used to describes the number solitons existing inside the MRR. Different soliton states will lead to different patterns on the observable optical spectrum of the frequency comb.

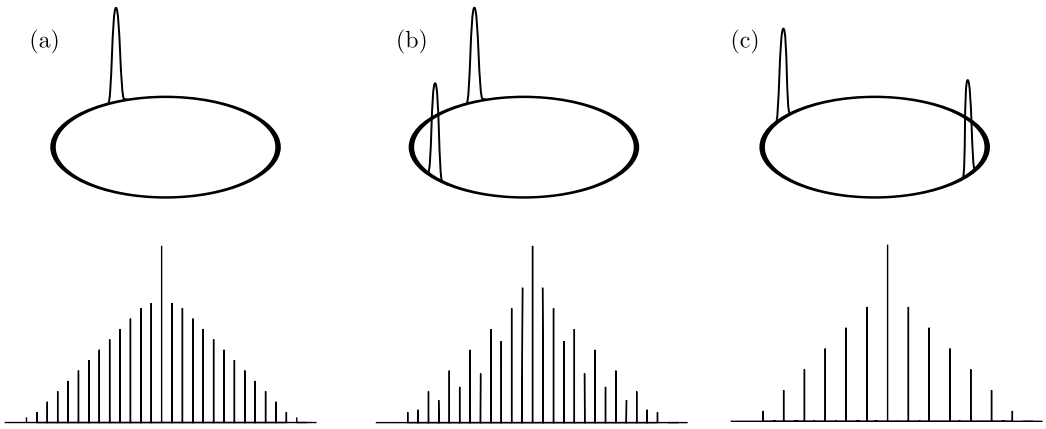

Figure 5.2: Illustration of different soliton states and the corresponding optical spectra of the frequency comb for (a) Single soliton state, (b) multi-soliton state, and (c) two FSR comb (special case of the multi-soliton state).

When we have only one soliton existing within the MRR the state is called a single soliton state. This state produces a coherent frequency comb known as a single soliton comb which will have a characteristically $sech^2$ shape that other soliton states do not exhibit. Any other state with more than one soliton circulating

inside the MRR is known as a multi soliton state. Multi-soliton states can result in many different comb spectra depending on the number of solitons and their angular distribution within the MRR. In multi-soliton states there will be interference between the different comb lines which will result in characteristic patterns in the optical spectrum of the frequency comb [12]. Figure 5.2 depicts three different soliton states (a) single soliton state, (b) multi-soliton state, and (c) multi-soliton state with evenly spaced solitons.

5.2 Experimental Setup

Comb generation in MRRs are highly dependent on, not only the MRR properties such as dispersion and Q-values, but also the pump parameters, i.e. pump power and frequency detuning (i.e. the relative shift in pump frequency compared to the cavity resonance of the MRR). When generating a comb on the other hand, high pump powers are needed in order to initiate the cascaded FWM necessary to create the comb lines.

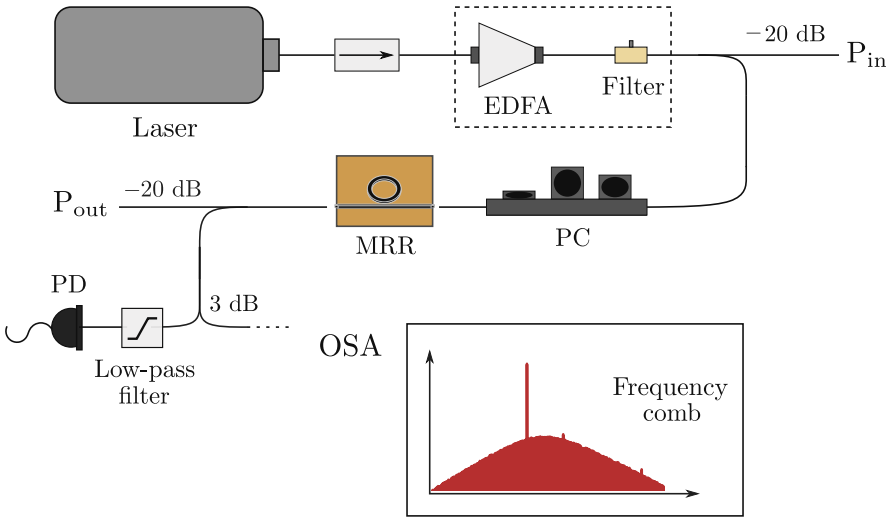

Figure 5.3: Schematic overview of the fibre coupled frequency comb generation setup. The setup uses two lasers at different times: (1) Toptica DLC pro and (2) NKT Koheras BASIK (is not sent through the EDFA and pump filter). The laser output is coupled to the MRR using tapered fibres. The output of the MRR is divided into two using a 3 dB coupler. One part is used to create the soliton trace signal by filtering out [high/low] frequencies. The other output is connected to an OSA and shows the generated comb. All the fibres in the setup are single-mode fibres. EDFA: Erbium-doped fibre amplifier, PC: Polarisation controller, PD: Photodetector, OSA: Optical spectrum analyser.

To initiate the formation of solitons and the generation of a frequency comb the MRR must be pumped using a CW laser. In our experiments we have tested the outcome using the different CW pump lasers: (1) Toptica DLC pro and (2) NKT Koheras BASIK. The Toptica has a lower output power and the output is therefore sent through an EDFA in order to amplify the signal. After the EDFA a filter is inserted to filter out (block) the pump light for the EDFA. The output power of the Toptica after it has been amplified is controlled using an attenuator. The EDFA and filter are not necessary when using the NKT since it has an output power of 80 mW which is sufficient to initiate the formation of solitons.

For the majority of our measurements the NKT was directly connected to the -20 dB coupler. It was however, for comparison reasons, connected in the same manner as the Toptica for some of the measurements. A schematic overview of the setup we used to create soliton signal and for the generation of frequency combs can be found in Figure 5.3. The whole setup is fibre coupled using single mode fibres.

The laser (amplifier) output is connected to a -20 dB splitter. The -20 dB output of the splitter serves as a monitor for the input power sent to the chip. The main output is sent through a polarisation controller to the MRR chip. From here it is coupled into the MRR, in the same way as for the dispersion measurements, using tapered lensed fibres. The light coupled of the chip after the MRR is first connected to a -20 dB coupler in order to read out the output power and hereafter it is split in two using a -3 dB coupler. The one half of the signal is passed through a low-pass filter is used to filter out the pump signal in order to create the soliton trace signal which is detected on a photo detector which is connected to an oscilloscope. The other path is connected to an optical spectrum analyser (OSA) which measures the optical frequency spectrum of the generated frequency comb.

5.2.1 The Heater Signal

In order to create a soliton comb it is necessary to be able to effectively "catch" a soliton. The SiN platform used for this experiment has integrated heater elements that allows for thermally tuning of the resonance of the MRR as compared to tuning of the laser frequency. The heater is connected to a function generator provided with a heater signal. This signal is used to generate a soliton comb by thermally red-shifting the resonance. By changing the heater power we can change the temperature of the MRR making it expand (or contract) which will lead to a change in the cavity resonance frequency. By creating a red-shift we can make sure that we are on the right side of the resonance. When the power increases inside of the MRR the temperature will also increase. This will create a change in the refractive index and result in a shift in all the resonances inside of the cavity.

In order to achieve a linear scan of the temperature in time, the power to the heater should change linearly in time, neglecting for the moment the heating due to dissipated optical power and assuming that the temperature of the resonator

follows the heater power directly. Using the Joule heating of a resistor:

$$P = U \cdot I = R \cdot I^2, \tag{5.1}$$

the control voltage to the heater is chosen to have a parabolic shape for a linear ramp.

The implemented heating signal can be seen in Figure 5.4 (left). This arbitrary wave function creates an instant heating of the chip indicated by the first vertical line to the left in the plot. The heating is then stopped and the chip is slowly cooled down according to the quadratic function in Eqn. 5.1. The small kick-back step V_{back} at the end of the heating signal is used to stop the thermal tuning in order to stabilise the soliton comb. The kick-back is created by increasing the voltage by a small amount which allows us to tune back onto a soliton step without scanning over it by stopping the cooling process. The size of the kick-back is an important parameter. It largely determines whether or not we will catch a soliton. An illustration can be found in Figure 5.4 (right).

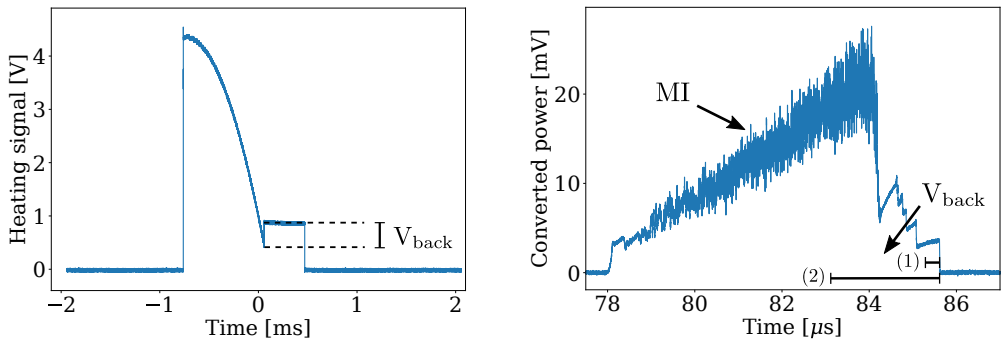

Figure 5.4: **(Left)**: Heating signal as a function of time. The parameter V_{back} controls the "kick-back" signal that is used to stabilise the soliton state. **(Right)**: A soliton trace signal generated using the 266-BSS1-I0p5 device that is used for comb generation.

If V_{back} is set to a too high of a value, scenario (2) in Figure 5.4 (right), we are most likely to be pushed back into the MI state. This will create a chaotic comb state whereas a smaller V_{back} allows for a better opportunity to be pushed back onto a soliton step. Although a small V_{back} is desired it can also be set too low. As a minimum V_{back} has to correspond to the length of a soliton step in order to push the system back into a soliton state. With a V_{back} corresponding to a shift in the trace signal along the x-axis that is smaller than the length of a soliton step, corresponding to (1) in the figure, it may not be possible to stop the thermal cooling of the chip in time and we will end up scanning over the resonance and the system will become thermally unstable.

The converted power trace used for comb generation is shown together with the heating signal in Figure 5.5. In (a) and (b) a zoom-in of the soliton trace signal

in the beginning and the end of the step formation are plotted, and in (c) the full soliton trace signal is shown together with the heater signal from the function generator. Here, it is clearly demonstrated how the heating signal allows us to stay on soliton step for a long period of time.

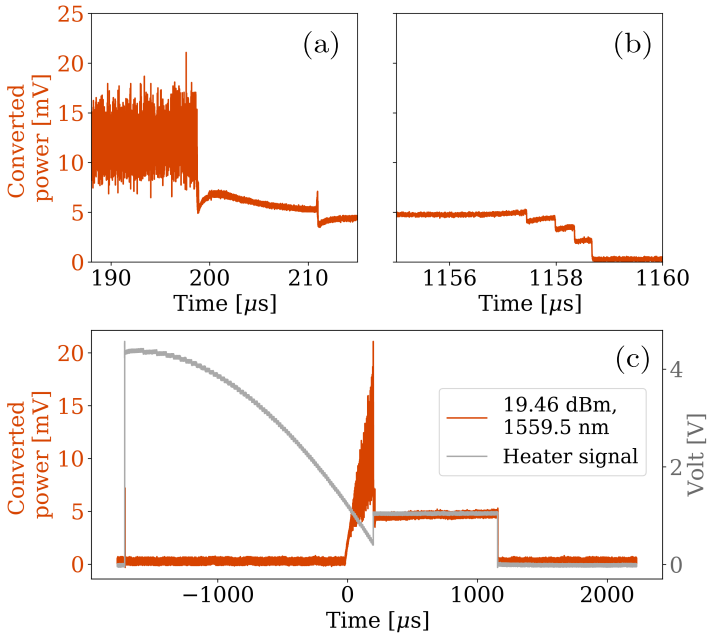

Figure 5.5: Converted power trace used for comb generation. (a)+(b) shows a zoom-in of the soliton steps and (c) shows the full trace along with the heater signal used to generate the soliton comb.

5.3 Soliton Step Length Dependencies

As mentioned earlier, the generation of frequency combs is among other dependent on the pump power. We decided to investigate this dependency by looking at the soliton step length as well as the resulting generated combs by using two different lasers with different linewidths to do so by way of comparison. The first laser used is the same laser that was used in the dispersion measurement setup, namely the Toptica DLC DL pro. It is an external cavity diode laser (ECDL) with a tunable range of approximately 100 nm and a linewidth of around 100 kHz. The other laser is a single frequency[1] Koheras BASIK E15 from NKT with a linewidth of < 0.1 kHz operating at 1542 nm with an output power of roughly 80 mW.

5.3.1 On-Chip Power

Based on the Toptica being a tunable laser it seemed evident to conduct measurements on more than one resonance in order to gain more information on how

[1]It has a tunable range of approximately 800 pm

the system behaves at different wavelengths. We chose the following resonances: 1541.8 nm, 1542.6 nm, 1554.7 nm, and 1559.5 nm. The soliton trace signal at different on-chip powers for two different resonances, 1541.8 nm and 1559.5 nm, can be found in Figure 5.6.

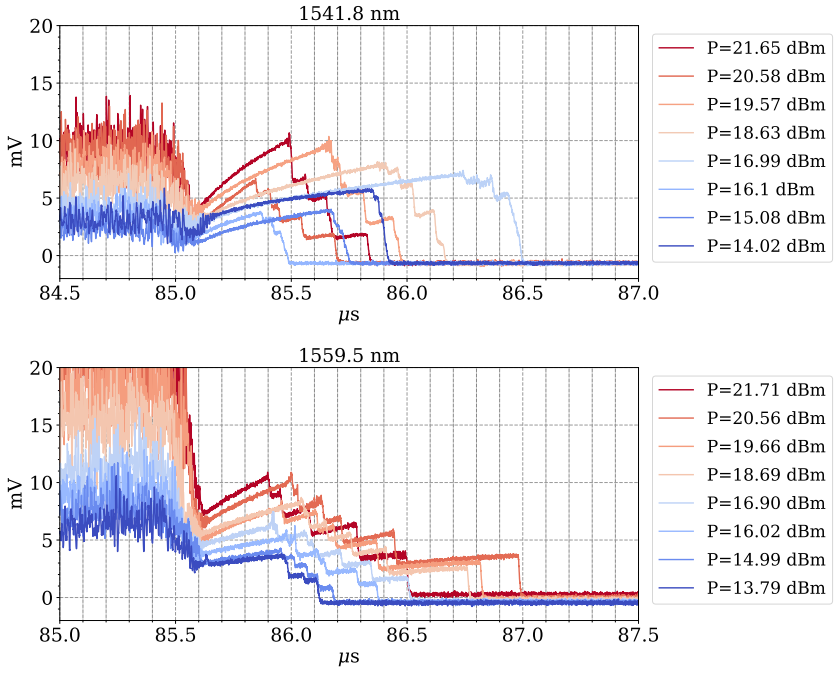

Figure 5.6: Single soliton trace signals at the resonances 1541.8 nm and 1559.5 nm shown for eight different on-chip powers. All the trace signals are obtained using the Toptica laser.

Comparing the two resonances in the figure the difference in both soliton step and power level length is very obvious. Where we in the traces for 1559.5 nm see a relation between input power P and the measured power level as well as distinct individual soliton steps, we do not observe the same behaviour at 1541.8 nm. At 1541.8 nm the individual steps are harder to distinguish and not all steps are visible for all of the input powers in the same way as there were at 1559.5 nm. We also do not see the same relation between input power and power measured on the oscilloscope when looking only at the step formation. As an example the longest total step length for the 1541.8 nm resonance is observed at $P = 16.99$ dBm.

In the same manner the different resonances is compared for the same on-chip power in Figure 5.7 for measurements from both the Toptica and the NKT lasers. For this specific measurement, the NKT traces are not amplified using the EDFA. The reasoning for this was to investigate the possibility of generating a comb at low input power using the NKT laser without amplifying the output signal.

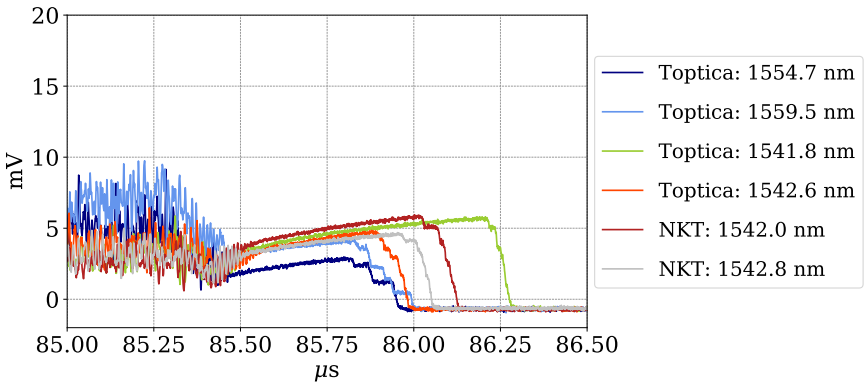

Figure 5.7: Comparison of the different resonances including traces from both the Toptica and the NKT laser at the same on-chip power (13.8 dBm).

We found the total soliton step length to vary with on-chip power, as is most apparent for 1554.7 and 1559.5 nm (shown in figure). In general the trace signal, as would be expected, increased as the on-chip power increased but so did also the individual soliton step lengths. In the trace shown for the 1559.5 nm resonance five distinct steps can be identified for all of the different on-chip power levels, except for the lowest one at $P = 13.79$ dBm. It is much more difficult to identify the same steps for the 1541.8 nm resonance (with the same applying to the 1542.6 nm resonance). In general, the converted power on the y-axis has a much lower value than that of the 1559.5 nm resonance.

This is most likely due to absorption in the MRR at those wavelengths. So even though we pump the MRR with more power, the output will not increase because of the material absorption which in general poses a problem when wanting to generate a DKS comb since the soliton step lengths decreases by a significant amount making it more difficult to reach a single soliton state.

Statistics

The soliton trace signal has a tendency to "flicker" (i.e. it rapidly moves back and forth). This means that we cannot form a complete idea of the total soliton step length by just looking at a single trace. The definition of the total soliton is the distance from t_{start} to t_{end} as seen in Figure 5.8. The total step length is determined using a running variance, i.e. the variance between neighbouring data points.

Between each scan the point of t_{start} and t_{end} will both randomly move back and forth but the biggest change is seen in the position of t_{end}. Looking at Figure 5.8 this could mean that at one scan t_{end} was located at 83 μs but at the next scan it could have moved to 82.5 μs. The typical total step length was around $0.5 - 1\mu$s.

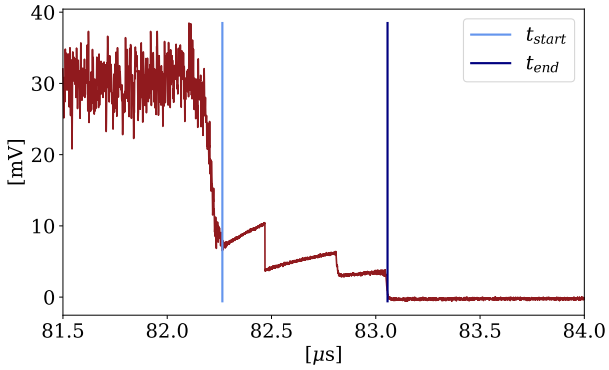

Figure 5.8: A single soliton trace signal showing the steps. The total soliton step length is defined as the part between t_{start} and t_{end}. The total step length observed using this device is on the order of a few μs.

Therefore, we saved a total of 100 consecutive scans of each of the traces for the different input powers in order to gain some statistics on the total step length and how it varies. In figures 5.9 and 5.10 the histograms of the total soliton step length are shown for the 1541.8 nm and the 1559.5 nm resonances at four different on-chip powers: highest, lowest, and two intermediate on-chip powers. The same histograms were made for the two other resonances at 1542.6 nm and 1554.7 nm.

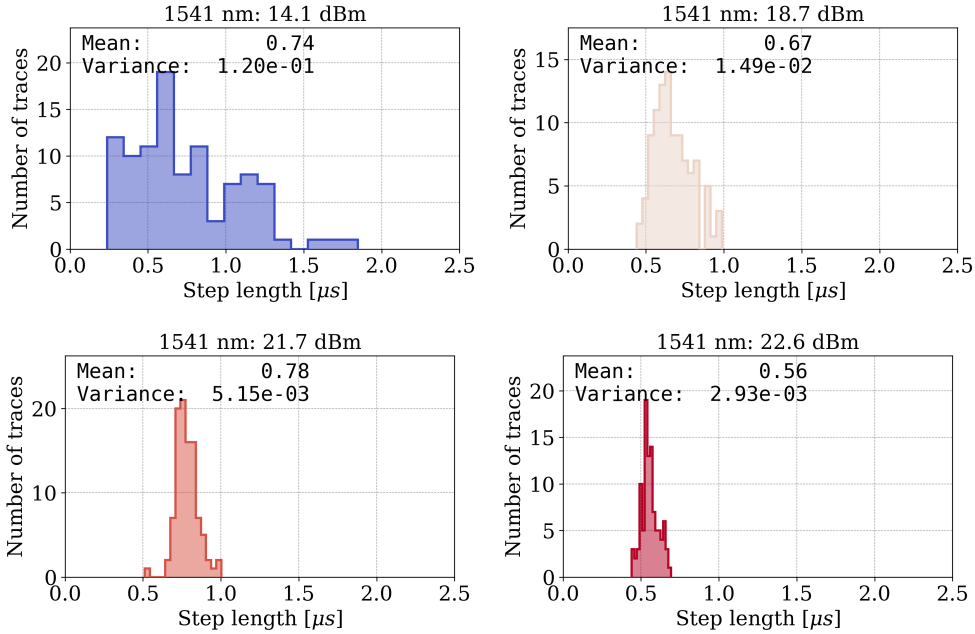

Figure 5.9: Histograms of the total soliton step length at 1541.8 nm for four different on-chip powers: 14.1 dBm, 18.7 dBm, 21.7 dBm, and 22.6 dBm.

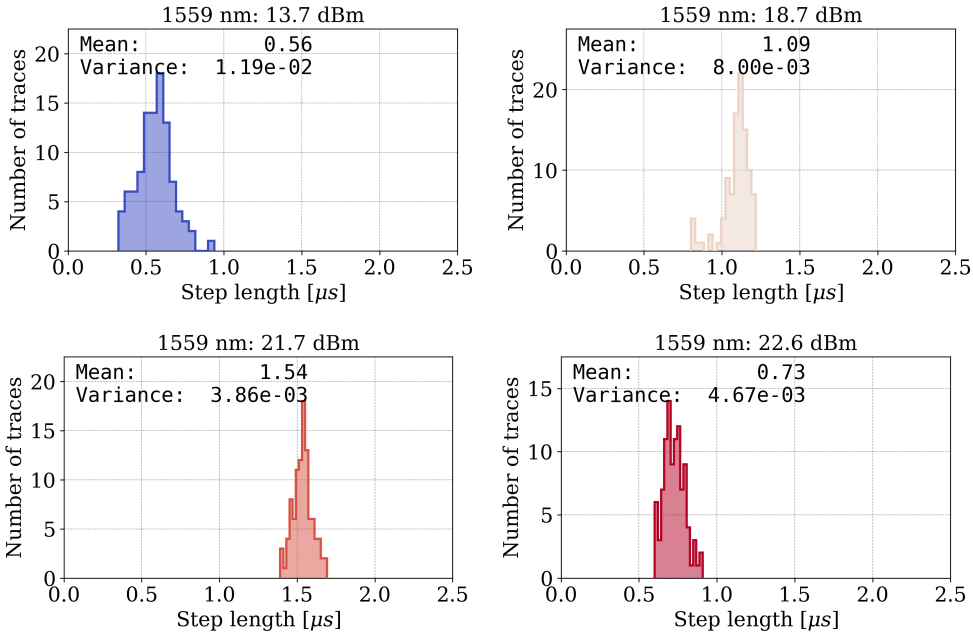

Figure 5.10: Histograms of the total soliton step length at 1559.5 nm for four different on-chip powers: 13.7 dBm, 18.7 dBm, 21.7 dBm, and 22.6 dBm.

For the 1541.8 nm resonances in Figure 5.9 we see that for the lowest input power there is a large variance (of around 0.12 μs) for the total step length compared to the two highest input powers which is on the order of 10^{-3} μs. In general, we do not detect an overall change in the mean value when applying higher on-chip powers. Looking at the same results for the 1559.5 nm resonance there seem to be less variance at the two lower on-chip powers. Compared to the same on-chip powers at 1541.8 nm they are on the order of a magnitude smaller. Also, at 1559.5 nm we see how the mean value of the total step length increases as the on-chip power is increased with the exception of the highest on-chip power (22.6 dBm) where there was a significant decrease in the mean total step length.

The 100 trace scans were used to calculate the average mean and variance of the total length of the soliton steps as a function of all the different on-chip powers at the different resonances for both the Toptica and the NKT. The results are shown in Figure 5.11.

Looking at the mean value of the two groups (i.e. 1540 nm and 1550 nm resonances) the same features found in Figure 5.6 of the soliton trace signal regarding the visibility of the soliton steps also become very prominent here. We achieve a much longer total soliton step length for the 1550 nm resonances which could imply that the individual step length increase. Although, from the traces in Figure 5.6 it appears as though the change mostly applies to the last soliton step, which means that it becomes easier to reach a single soliton state in comb generation.

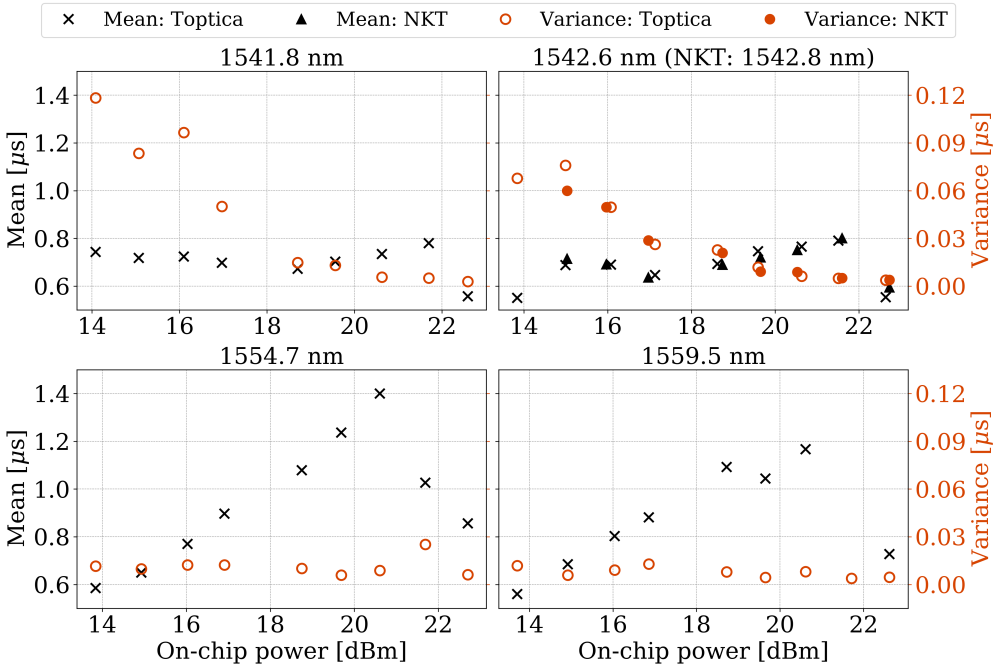

Figure 5.11: The averaged (100 scans) mean and variance of the total length of the soliton steps as a function of on-chip powers at different resonances.

The most noteworthy observation is that there seem to be an optimal on-chip power at which the total soliton step length is at the longest. For the two 1550 nm resonances this point appears around 21 dBm. For the 1540 nm resonances it is not as prominent but they all seem to have the feature at a slightly higher value, approximately around 21.5 dBm. Also, the fact that we do not see a rise in the mean values for the 1540 nm resonances in the same way as we do for the 1550 nm resonances supports the suspicion we had of material absorptions at those wavelength.

Comparing the obtained variances, there is a noticeable difference in the variance at lower input powers comparing the two 1540 nm with the two 1550 nm resonances. The difference seem to become insignificant at powers above 18 dBm. The most distinct difference when looking at the variance is that for the 1540 nm resonances it decreases as the on-chip power is increased whereas for the 1550 nm it is more or less constant over the full range of on-chip powers.

Lastly, comparing the results obtained at the same resonance using the Toptica and the NKT it is not apparent that the linewidth of the laser makes a difference for our results. The variance of the NKT is slightly lower at 15 dBm but since we do not have a measurement at 14 dBm with the NKT it is difficult to conclude whether or not a more narrow linewidth is preferable at lower on-chip powers.

5.3.2 Polarisation

The geometry of the device we have been working on is designed to support the TE polarisation. By this is meant that only light polarised in the TE direction will be highly confined whereas the other polarisation, TM, will have light leaking out of the MRR. So, besides the soliton step length being dependent on the input power it will also depend on the light coupled into the MRR having the correct polarisation. This is adjusted using the PC in the setup by suppressing the TM polarisation and thereby enhancing the correct polarisation of the light coupling into the MRR.

Although it is possible to generate a signal very similar to the soliton traces shown in Figure 5.6 using the wrong polarisation, it will not show the same characteristic soliton steps and for the same reason it cannot be used to generate a frequency comb. The soliton trace signal is shown in Figure 5.12 for the 1559.5 nm resonance at three different on-chip powers using the wrong polarisation.

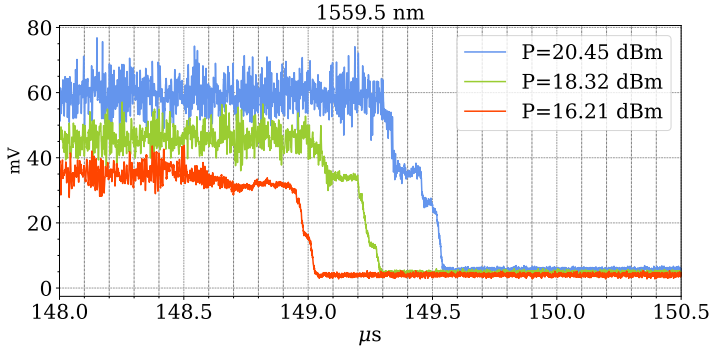

Figure 5.12: Soliton trace signals at the 1559.5 nm resonance for the TM ("wrong") polarisation shown for three different on-chip powers.

5.4 Experimentally Generated Combs in the SiN Microresonator

In this section we present the combs that have been generated in the SiN microresonator using the soliton trace signal presented in the previous section. Even though the heater signal can be used to "catch" the solitons by thermal tuning, the rapid flickering of the soliton trace signal makes it impossible for us to control on which step we land. This means, especially for low on-chip powers, that we rarely land on the single soliton step in the first try. At resonances with a prominent lower step, like the two 1550 nm resonances, the chances increases as it becomes easier to control using the V_{back}. We do not necessarily always know which step we are currently on, it should always be possible to tune the comb from a multi-soliton state into a single soliton step. By slowly tuning the laser frequency further to the red-detuned (increasing the wavelength of the pump laser) side we can move the

system to a "lower" soliton state until the single soliton state is reached.

For each of the combs we calculate the *conversion efficiency*. This figure of merit is used to describe how much of the pump power is converted into the comb. The conversion efficiency becomes especially important if the application of the generated comb is within the field of telecommunication in which single comb lines are used as carriers to process signals. But in general it the conversion efficiency is used to describe the performance of the MRR. It is calculated by taking the total comb power (without the pump) and dividing that with the on-chip power:

$$\eta = P_{comb}/P_{in}. \tag{5.2}$$

5.4.1 Comb Generation using the Toptica

In this section we present a selection of the combs generated with the Toptica at the same four resonances as was presented in section 4.2. Overall the combs generated at the two 1540 nm resonances was observed to exhibit similar behaviour and the same is true for the two 1550 nm resonances.

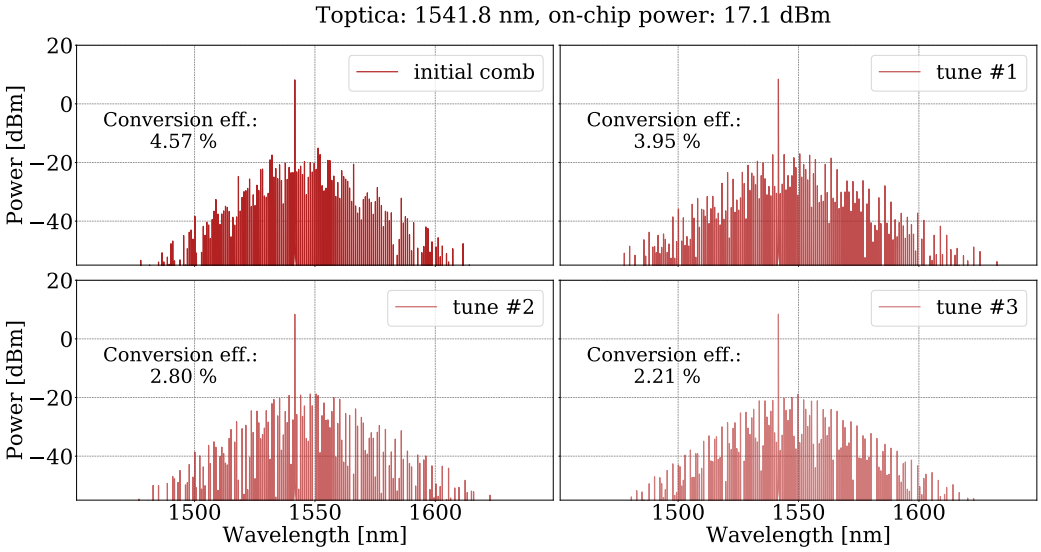

Figure 5.13: A multi-soliton comb generated at 1541.8 nm using the Toptica DLC pro with on-chip power of 17.1 dBm. The figure shows the initial (multi-soliton) comb and the three subsequently states that was reached by tuning the pump laser.

Figure 5.13 shows the typical generation of a frequency comb at 1541.8 nm for an on-chip power of 17.1 dBm. The comb structure and tune behaviour shown in this plot is representative for both of the 1540 nm resonances but the comb shown for the third tune (tune #3) represents the closest we came to a single soliton comb at the 1540 nm resonances. Both these resonances had very similar behaviour and we did not succeed with any comb generation in neither of the 1540

nm resonances above an on-chip threshold of around 18 dBm nor did we succeed in generating a single soliton frequency comb. The explanation is probably once again to find in the material absorptions as we also observed in Figure 5.11. Even with higher pump powers we did not see any increase in neither the output power of the transmission nor the length of the individual soliton steps.

Looking at the soliton trace signals in Figure 5.6 for the 1541 nm resonance, we clearly see that the step corresponding to the single soliton state is hardly present for on-chip powers below 18 dBm. This can help us explain why we cannot seem to generate combs at lower on-chip powers at these resonances. At low on-chip powers it can be more challenging because the thermal tuning is likely to be larger than the tuning of the laser frequency. So, when we tune the laser frequency we end up tuning over the resonance which will cause the whole system to become unstable. In general, when we tuned the laser frequency it was done at as small steps as possible ($\sim 1 - 10\mu$m) and, especially at lower on-chip powers, after each tune the system was allowed some time to thermally stabilise before further tuning.

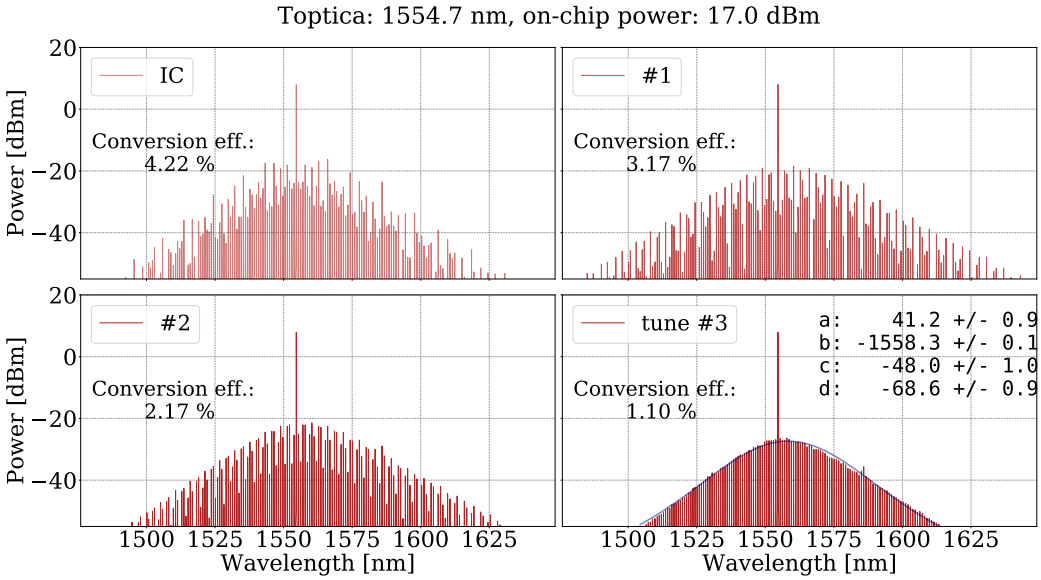

Figure 5.14: The initial multiple soliton comb that was tuned into a single soliton state. The bottom right plot shows a single soliton comb generated at 1554.7 nm using the Toptica DCL pro. On-chip power is 17.0 dB IC: Initial comb.

With the two 1550 nm resonances single soliton comb generation was observed frequently and even at lower on-chip powers it was possible to tune the combs from a multi-soliton state into a single soliton. This is also supported by the soliton trace signals shown in Figure 5.6. Here, the 1559.5 nm resonance exhibits the most distinct steps, even at the lowest of the on-chip powers, compared to. In Figure 5.14 it is illustrated how the initial comb generated at 1554.7 nm was tuned into a single soliton comb. The on-chip power is 17.0 dBm which is the same

on-chip power that was used to generated the comb shown in Figure 5.13. The single soliton comb is fitted to a $sech^2$ using the function:

$$F(x) = a \cdot \text{sech}^2\left(\frac{x + \text{peak}}{\text{width}}\right) + b, \tag{5.3}$$

where the parameter P is used to describe the peak value of the curve, W is related to the width, and the height of the curve is the sum of the parameters a and b.

Although both of the 1550 nm resonances perform much better than the two 1540 nm resonances, comparing the two resonances, we did observe that in general the best results were obtained when pumping the device at 1559.5 nm even though the soliton trace signals are very similar for the two. At 1559.5 nm, there was easy access to what appears to be single soliton states and slightly broader combs could be realised as is shown in Figure 5.15.

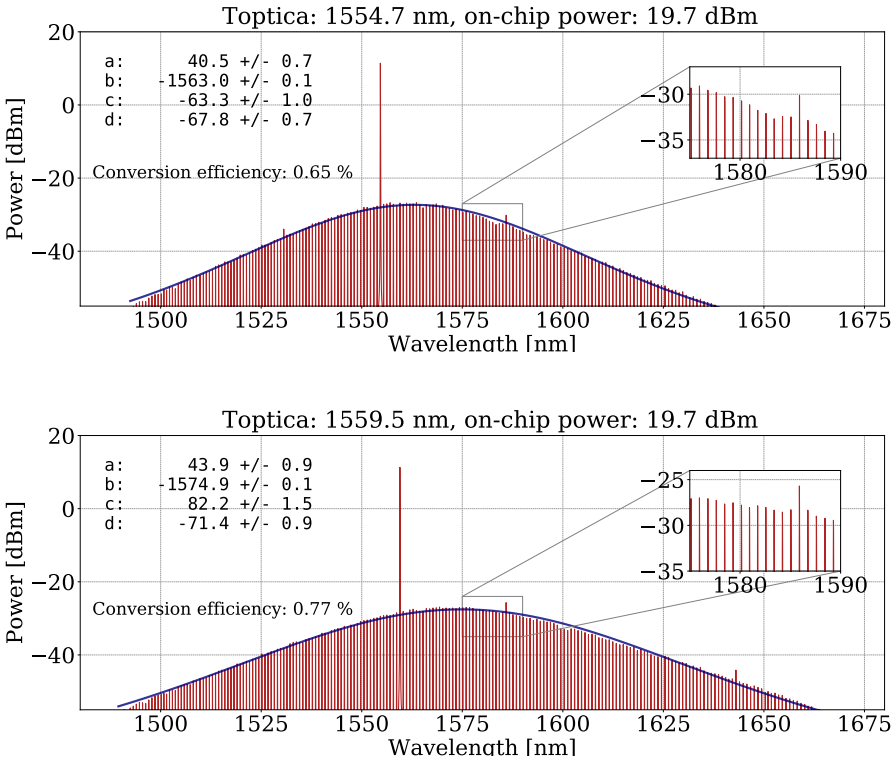

Figure 5.15: **(Above)** single soliton comb generated at 1554.7 nm spanning from approximately 1490 nm to 1635 nm. The on-chip power is 19.7 dBm. **(Below)** using the same on-chip power, a single soliton comb generated at 1559.5 nm spanning from approximately 1490 nm to 1665 nm.

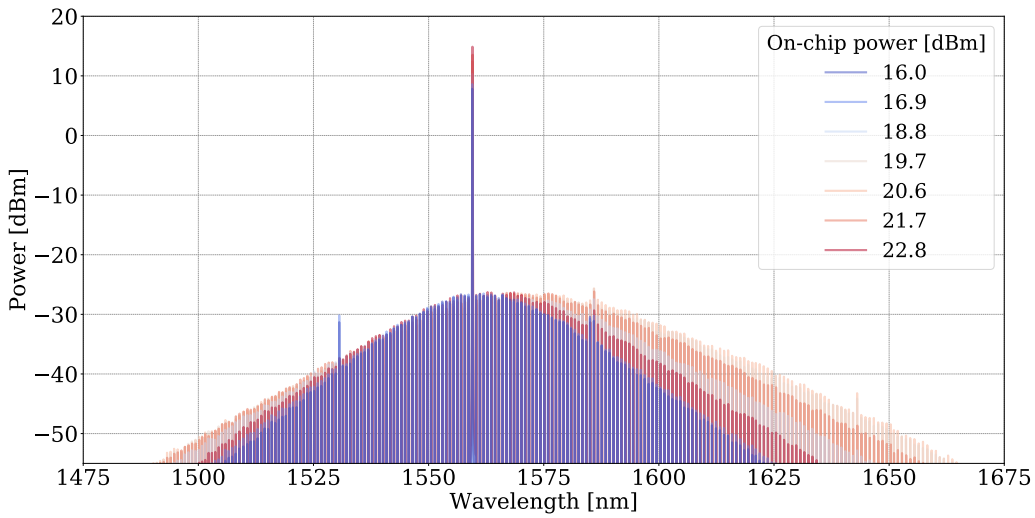

Figure 5.16: Comb spectra showing all the different on-chip powers at which a single soliton state was reached using the 1559.5 nm resonance.

For both of the 1550 nm resonances it applies that single soliton combs could only be generated at on-chip powers of 16 dBm and up. But, the same trend that was observed in Figure 5.11 is also observable in the generation of combs where there seem to be an optimal on-chip power. Above that threshold power the step size begins to decrease. When generating the combs it is also present and can be seen as a narrowing of the span of the spectrum as shown in Figure 5.16.

Raman Effect

Another distinct feature that can be observed from the plot in Figure 5.16 is a red shift of the center value of the $sech^2$ shape of the spectra from the pump frequency. This feature is the result of the Raman effect caused by a vibrational material response of the third order nonlinearity in the MRR. Like the other effects, it can be accounted for in the NLSE by including an extra term:

$$\frac{\partial A}{\partial z} - \frac{i}{2}\beta_2\frac{\partial^2 A}{\partial t^2} - \frac{\alpha}{2} - i\gamma\left(|A|^2 A - T_R A\frac{\partial |A|^2}{\partial T}\right) = 0, \tag{5.4}$$

where the parameter T_R describes the slope of the Raman gain spectrum which occurs due to the stimulated Raman scattering in the medium. This term that have now been introduced in Eqn. 5.4 is the term responsible for the self-frequency shift [2].

The Raman effect causes a continuous shift of the soliton as it propagates inside the MRR leading to a global shift of the whole spectrum. Karpov et al. found in [8] that the spectral red-shift increased as the pump laser was tuned from the blue side to the red over the entire range in which the soliton exists, i.e. the soliton step. This effects can also be observed in Figure 5.16. We see how the spectrum

shifts further to the red side compared to the pump at the pump power is increased which is also where the longest single soliton steps are found (Figure 5.6). This is due to the thermal heating of the ring caused by the higher intensities.

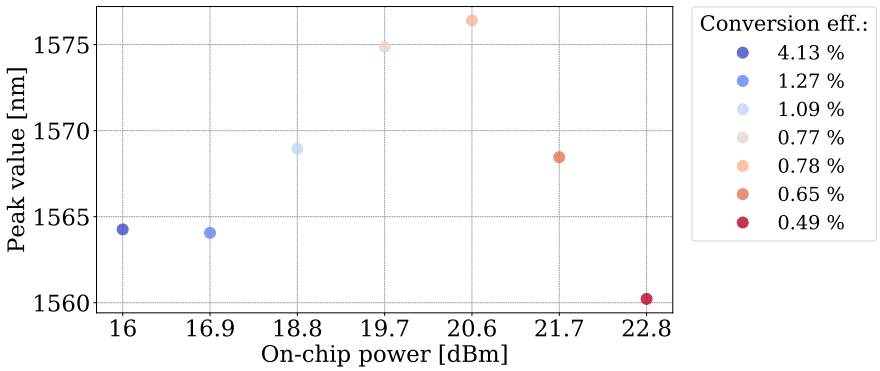

Figure 5.17: The shift in peak power of the $sech^2$ spectrum as a function of the same on-chip powers shown in Figure 5.16.

Figure 5.17 shows the peak values obtained from fitting the spectra shown in Figure 5.16 to the $sech^2$ function in Eqn. (5.3). It shows how the peak moves from around 1564 nm for the 16 dBm on-chip power and goes all the way up to 1576 nm for 20.7 dBm. After 20.7 dBm the value decreases again in correspondence to the decrease we also saw when looking at the soliton step lengths.

5.4.2 Comb Generation using the NKT

The NKT laser operates in a narrow wavelength span around 1542 nm which already has been illustrated to be a tricky area due to the absorption in the MRR[2]. But even though we did not successfully generate any single soliton combs using the Toptica laser we still wanted to see if the narrower linewidth of the NKT would make a difference in the generation of combs. In order to increase the output power of the NKT, in the same way we were able to do it with the Toptica, it was connected to the EDFA.

[2]At best we are able to reach two different resonances, corresponding to the 1541.8 nm and 1542.6 nm using the NKT, by tuning the laser frequency. In theory we could also increase/decrease the temperature of the ring which also should allow us to reach other resonances but this was not done in this experiment.

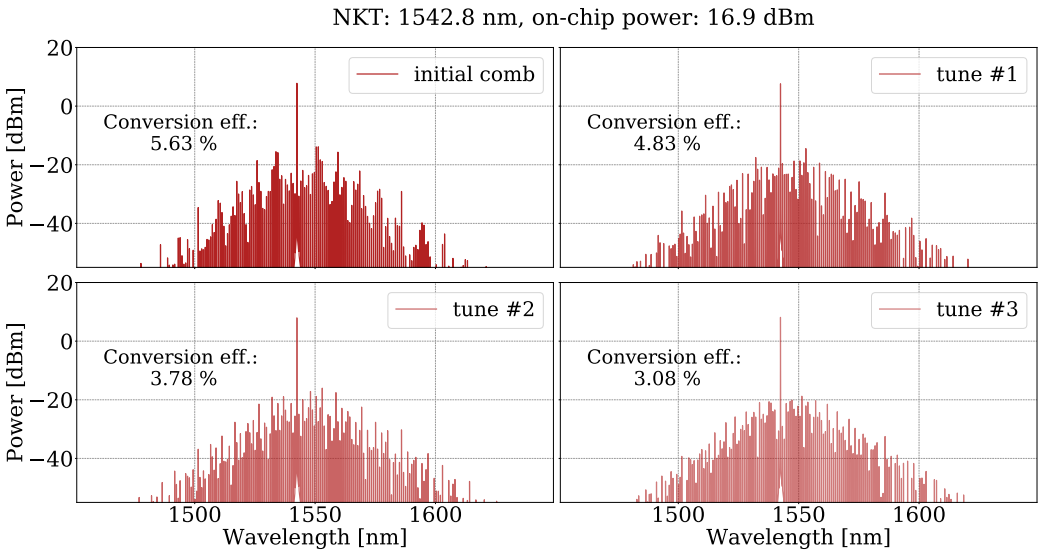

Figure 5.18: A multi-soliton comb generated at 1542.8 nm using the NKT Koheras BASIK with on-chip power of 16.9 dBm. The figure shows the initial (multi-soliton) comb and the three subsequently states that was reached by tuning the pump laser.

Comparing the two different combs that we generated at this specific on-chip power using the two lasers we do not see any significant improvement when using a laser with a more narrow linewidth at the 1542 nm wavelengths. Actually, it would rather appear that when just comparing these two results that the Toptica performed better. But, the results in Figure 5.13 were the best results we obtained at this wavelength and it cannot be excluded that similar results could be produced using the NKT. The system is very sensitive at this wavelength and in general we had to be very careful when tuning the laser frequency due to the very narrow steps.

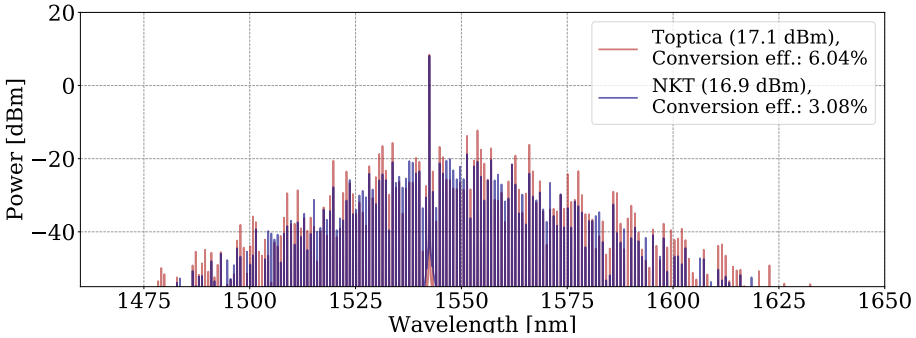

Figure 5.19: Multi-soliton combs generated at the same on-chip power using two different lasers. The red spectra shows the Toptica at 17.1 dBm and the blue shows the NKT at 16.9 dBm.

In Figure 5.18 we compare two combs generated at the same on-chip power for the same resonance using the NKT and Toptica lasers. The red spectrum is generated at 1542.6 nm using the Toptica laser and the dark blue spectrum is the same as shown bottom right in Figure 5.18 for the NKT at 1542.6 nm.

Here, we do see a large difference when we compare the NKT results with the comb generated at 1542.6 nm using the Toptica (corresponding to the same resonance). Comparing these two spectra, the converison efficiency is twice as high for the Toptica which means that less of the pump light is converted into the comb. But it is hard to conclude much from these results since we cannot be certain that it is not possible to obtain better results for the Toptica using this resonance.

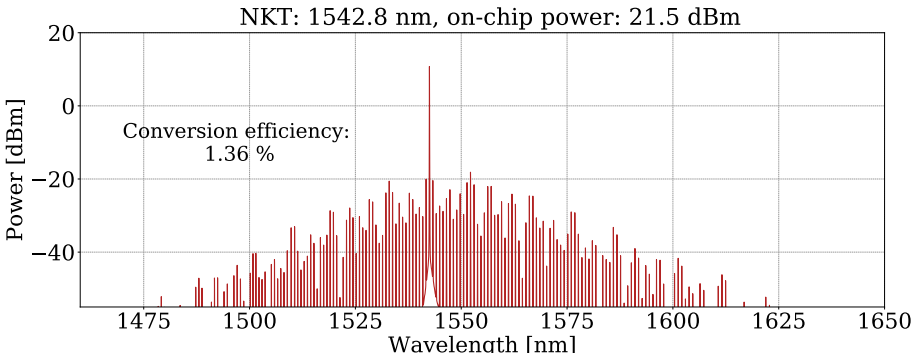

Figure 5.20: A multi-soliton comb generated at 1542.8 nm using the NKT Koheras BASIK with on-chip power of 21.5 dBm.

One noticeable difference between the lasers was that we were able to go to much higher on-chip powers when using the NKT. With the NKT laser we managed to generate combs at all of the tested on-chip powers with the highest being 22.7 dBm. The higher on-chip powers did not enable us to generate single soliton combs but from the results obtained from the soliton trace signals in Figure 4.13 we did expect that either. A comb generated at 21.5 dBm using the NKT laser can be seen in Figure 5.20.

Chapter 6

Frequency Stability Analysis

It can be difficult to tell, at first glance, whether or not a comb generated using one laser is in anyways performing better than a comb generated using a different laser as they can appear very similar. There are many factors that can introduce different types of noise to the system and we cannot measure these directly from just the comb spectra alone.

What can be done, is measuring the stability of the two lasers used for comb generation in order to compare with the stability of the generated combs. This can give an idea of what types of noise are affecting the system at different frequency scales. Also, by comparing different stability measurements the hope is that we are able to form an idea of the origins of noise.

The stability of any frequency source can be assessed by looking at how the source fluctuates in frequency over a period of time. This will then tell to what degree the source is stable in a given window of time.

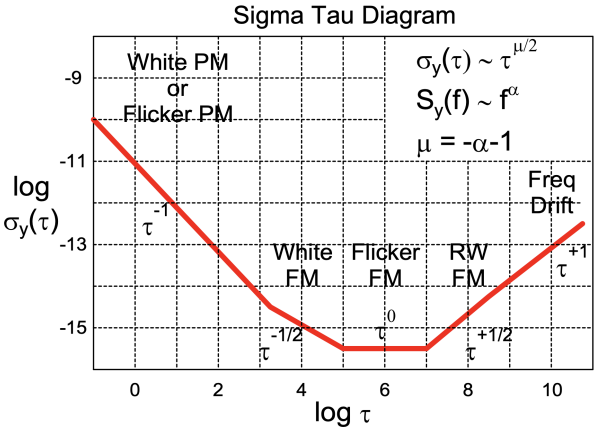

Figure 6.1: Sigma-tau diagram adapted from [22].

A common way of presenting the frequency stability in the time domain is by a *sigma-tau* plot (log-log plot) which measures the stability as a function of aver-

aging times over which the stability has been measured (see Figure 6.1. Presented this way, in a sigma-tau plot, different types of noises can be identified due to their characteristic slope. As an example, if we have a system that is completely dominated by white noise (or any other uncorrelated measurement), then we can decrease the uncertainty by taking more measurements. This corresponds to a negative slope proportional to $\tau^{-1/2}$.

6.1 Allan Variance

We measure the frequency stability by applying a two-sample variance method known as the *Allan variance* $\sigma_y^2(\tau)$. It is worth noting that the results typically would be expressed in terms of the *Allan deviation* which is the square root $\sigma_y(\tau)$. Mathematically, it is defined as:

$$\sigma_y^2(\tau) = \frac{1}{2(M-1)} \sum_{i=1}^{M-1} \left[y_{i+1} - y_i \right]^2 , \tag{6.1}$$

where y_i describes the ith element of M measurements each of which are the averaged frequency over a time (measurement) interval τ, that spans over a total measurement time, T. Several version of the Allan variance exists here among the overlapped and the modified Allan variance [22].

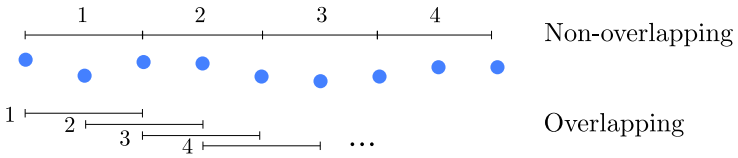

Figure 6.2: Illustration of the difference between a non-overlapping and an overlapping sampling.

The overlapping Allan variance (AVAR) is one of the most commonly used methods of frequency stability. Instead of averaging individually over larger sampling sizes, AVAR is used to create overlapping rolling sample for each averaging time τ using all possible configurations as shown in Figure 6.2. For a data set containing M measurements for an averaging time of $\tau = m\tau_0$ the frequency stability is given by the expression:

$$\sigma_y^2(\tau) = \frac{1}{2m^2(M-2m+1)} \sum_{j=1}^{M-2m+1} \left[\sum_{i=j}^{j+m-1} \left(y_{i+m} - y_i \right) \right]^2 \tag{6.2}$$

The modified Allan variance (MVAR) is sometimes used instead of the AVAR due to its ability to distinguish between white PM noise and flicker PM[1] noise.

[1] Phase modulation

The expression for MVAR is:

$$\mathrm{Mod}\sigma_y^2(\tau) = \frac{1}{2m^4(M-3m+1)} \sum_{j=1}^{M-3m+2} \left[\sum_{i=j}^{j+m-1} \left\{ \sum_{k=i}^{i+m-1} (y_{k+m} - y_k) \right\} \right]^2 \quad (6.3)$$

6.2 Experimental Results

As mentioned the frequency stability is estimated from measuring the beat note of two frequency samples, which is equal to the difference in frequency between the two. This means that we have to make sure that the samples overlap. A 3 dB coupler is used to combine the two frequency samples into a single output port that can be connected to a spectrum analyser. When beating one of the comblines in the frequency comb with a laser, a filter is used to filter out all other frequencies than the one corresponding to the output of the laser. It can be convenient to start by adjusting the overlap of the samples on the optical spectrum analyser (OSA), used to measure the spectra of the frequency combs, but in order to get a clear view of the actual beat note we use an electrical spectrum analyser (ESA). The ESA shows the radio freqency (RF) spectrum of the combined output.

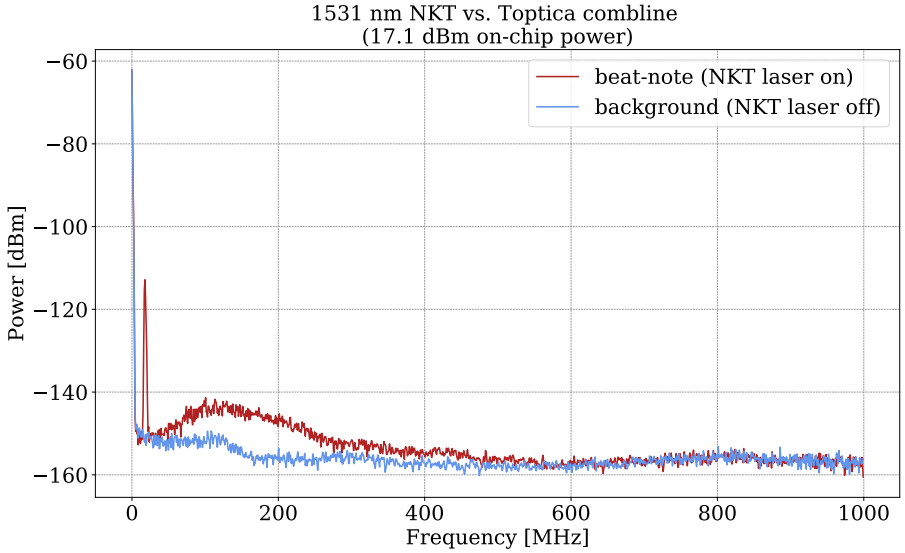

Figure 6.3: The RF spectrum of a beat note between a Toptica combline and the 1531 nm NKT laser. The Toptica comb is generated at 1559 nm using an on-chip power of 17.1 dBm.

The blue signal corresponds to the background signal, i.e. the signal of the full comb spectra when we turn off the NKT laser. The red signal shows the beat note between a Toptica combline at 1531 nm (filtered out) and the 1531 nm NKT laser.

To measure the beat note the output was connected to a a Pendulum CNT-90 frequency counter with an averaging time of 10 μs. We measured the beat note of the two NKT lasers with and without the EDFA. The NKT lasers are more stable than that Toptica, so these measurements were used as a standard of comparison to our other frequency stability measurements with the Toptica. The direct output of the Toptica was beat with both of the NKT at their respective output power and lastly we also measured the frequency stability of a combline generated using the Toptica compared to the 1531 nm NKT laser (Figure 6.3).

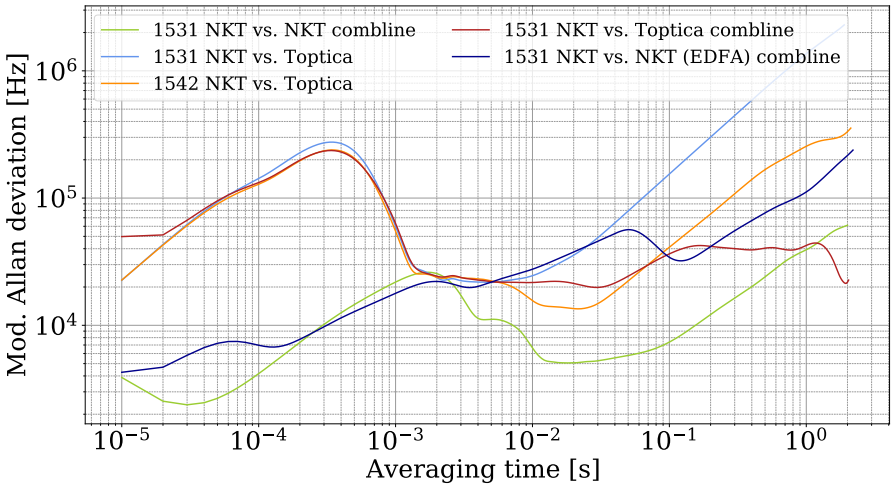

Figure 6.4: A modified Allan deviation comparing the frequency stability of the Toptica and NKT lasers used for frequency comb generation.

The Allan deviation is calculated using the **allantools** package in Python. The results are shown Figure 6.4 and from the results we see a trend in the measurements on the Toptica laser and they all overlap especially at averaging times below $\tau = 10^{-2}$. As expected, we also observe the NKT lasers to be more stable at shorter averaging times. From this we can also conclude that the instabilities we observe in our system is dominated by that of the Toptica and not the NKT.

Chapter 7

Conclusion

The work presented in this thesis has focused on the characterisation as well as the possibilities within frequency comb generation using a SiN integrated platform.

First and foremost, we have investigated the dispersion of the Wafer-266-BSS1-I0p5 device as well as characterised the device according to its Q-value and avoided mode-crossings. Six avoided mode-crossing was identified and the device was found to have an FSR of 100.2882 ± 0.0001 GHz and a β_2-value of -62.5 ± 0.4 ps^2/km. The average intrinsic Q of the device was found to be around $12 \cdot 10^6$. All of our results are in accordance with the results obtained by Ye et. al in [27]. For a similar MRR they report an FSR of 100 GHz, a β_2 of -67 ± 1 ps^2/km and an average intrinsic Q of $12.5 \cdot 10^6$.

For these measurements we have proposed a method of characterisation which allows for the use of a simple, dispersion free, source of reference using a free space cavity. We found that HOMs in the free space cavity can be used as additional reference points, artificially creating an even longer cavity. From this we can conclude that the free space cavity we used for our experiments could easily be replaced by a shorter cavity without loosing significant information regarding the dispersion measurements.

Secondly, we investigated the frequency comb generation in a MRR based on the intracavity formation of optical solitons. The formation of solitons is observed through the soliton trace signal in which each soliton step represents a different comb state. We found the soliton step lengths to vary at the different resonances but the total step length was also found to have a strong correlation with the on-chip power. The total soliton step length increases with the on-chip power up until it reaches an optimal on-chip power which was found to be around 21 dBm. After this point, there is a sharp decrease in the total step length.

Of the four resonances investigated, the two at 1554.7 and 1559.5 nm yielded the best results. Due to absorption around 1540 nm, the resonances at 1541.8 nm and 1542.6 nm, did not exhibit the same behaviour as we saw around 1550 nm. Even though the variance decreased at higher on-chip powers, for the 1540 nm, we did not observe a noticeable difference in the mean value of the total step length

neither for the Toptica laser nor the narrow linewidth NKT laser.

The same tendencies apply for the experimentally generated combs. Here, we only achieved a single soliton state pumping the MRR around 1550 nm. We were, however, able to generate what appears to be single soliton frequency combs at on-chip powers down to 16.0 dBm by tuning the laser frequency in order to reach lower steps in the trace signal. We also found that even though we could not distinguish between the Toptica and NKT in the results obtained from the measurements on the soliton trace signal we did see a difference when generating combs. Using the Toptica we were not able to generate combs above 18 dBm on-chip power but with the NKT laser we did not have that limitation. This could be related to what we found in the frequency stability analysis. Here, we concluded that it is the noise coming from the Toptica that is inherent for the system. Especially at lower averaging times the NKT had a MDEV that was an order of a magnitude smaller than the Toptica which means that the NKT has a more stable frequency output than the Toptica.

7.1 Outlook

The work presented in this thesis has been focusing primarily on the characterisation and analysis of the properties of the Wafer-266-BSS1-I0p5 device with the purpose of using it for efficient frequency comb generation. For the measurements we have showed here, no work was put into stabilising the system which means that we have no immediate control over the life span of a generated comb. The combs generated at the 1550 nm resonances typically has a life span of anywhere between 10 min and an hour. This was of course more than sufficient for our measurements but if the comb is to be used as a reference source in another setup it would be preferable to have longer life spans. This can be achieved by stabilising the system in which the frequency comb is generated.

One way could be by building a stabilisation scheme for stabilising the pump laser. In this scheme the laser frequency is controlled by a feedback loop that creates an error signal by measuring the output frequency compared to a reference. The error signal is used as the feedback for laser source in order to correct any drift in frequency.

Another way is to thermally stabilise the MRR by controlling the heater output such that any drift in the resonance frequency could be detected and counteracted by either increasing or decreasing the temperature. By stabilising the system in some way, regardless of the method, it becomes possible to stay in a single soliton state for a longer period of time which automatically leads to a longer life span of the frequency comb.

It could be interesting to setup up a simulation using the parameters from our setup such that we can compare the experimental result with the theory. This would maybe help us increase our understanding of system as an entity. We have already derived the equations needed for such a simulation but there are existing scripts that can be found online as well.

Bibliography

[1] Imad H. Agha, Yoshitomo Okawachi, and Alexander L. Gaeta. Theoretical and experimental investigation of broadband cascaded four-wave mixing in high-q microspheres. *Opt. Express*, 17(18):16209–16215, 08 2009.

[2] Govind P. Agrawal. *Nonlinear Fiber Optics*. Academic Press, third edition edition, 2001.

[3] Matthew Borselli, Thomas J. Johnson, and Oskar Painter. Beyond the rayleigh scattering limit in high-q silicon microdisks: theory and experiment. *Opt. Express*, 13(5):1515–1530, Mar 2005.

[4] Scott Diddams. Fundamentals of frequency combs: What they are and how they work. NIST, 2015.

[5] Tara Fortier and Esther Baumann. 20 years of developments in optical frequency comb technology and applications. *Communications physics*, 2(1):1–16, 2019.

[6] Martin Romme Henriksen. *Optical Frequency References*. PhD thesis, University of Copenhagen, 2019.

[7] Wenxian Hong. Design and characterization of a littrow configuration external cavity diode laser.

[8] Maxim Karpov, Hairun Guo, Arne Kordts, Victor Brasch, Martin H. P. Pfeiffer, Michail Zervas, Michael Geiselmann, and Tobias J. Kippenberg. Raman self-frequency shift of dissipative kerr solitons in an optical microresonator. *Phys. Rev. Lett.*, 116:103902, 03 2016.

[9] Maxim Karpov, Martin H. P. Pfeiffer, Hairun Guo, Wenle Weng, Junqiu Liu, and Tobias J. Kippenberg. Dynamics of soliton crystals in optical microresonators. *Nature Physics*, 15, 2019.

[10] T. J. Kippenberg, R. Holzwarth, and S. A. Diddams. Microresonator-based optical frequency combs. *Science*, 332(6029):555–559, 2011.

[11] Tobias J. Kippenberg, Alexander L. Gaeta, Michal Lipson, and Michael L. Gorodetsky. Dissipative kerr solitons in optical microresonators. *Science*, 361(6402), 2018.

[12] Lugiato LA, Prati F, Gorodetsky ML, and Kippenberg TJ. From the lugiato–lefever equation to microresonator based soliton kerr frequency combs. *Phil. Trans. R. Soc. A*, 376, 06 2018.

[13] Kevin Luke, Yoshitomo Okawachi, Michael R. E. Lamont, Alexander L. Gaeta, and Michal Lipson. Broadband mid-infrared frequency comb generation in a si3n4 microresonator. *Opt. Lett.*, 40(21):4823–4826, 11 2015.

[14] S. Wabnitz M. Haelterman, S. Trillo. Dissipative modulation instability in a nonlinear dispersive ring cavity. *Optics Communications*, 91(5,6):401–407, 02 1992.

[15] P. Meystre and M. Sargent 111. *Elements of Quantum Optics*. Springer, third edition edition, 1999.

[16] Kenji Nishimoto, Kaoru Minoshima, Takeshi Yasui, and Naoya Kuse. Investigation of the phase noise of a microresonator soliton comb. *Opt. Express*, 28(13):19295–19303, 06 2020.

[17] R. Paschotta. article on 'frequency combs' in the encyclopedia of laser physics and technology, 1. edition october 2008, wiley-vch.

[18] R. Paschotta. article on 'group velocity dispersion' in the encyclopedia of laser physics and technology, 1. edition october 2008, wiley-vch.

[19] A. Pasquazi, M. Peccianti, L. Razzari, D. Moss, S. Coen, M. Erkintalo, Y. K. Chembo, T. Hansson, S. Wabnitz, Pascal Del'Haye, Xiaoxiao Xue, A. Weiner, and R. Morandotti. Micro-combs: A novel generation of optical sources. *Physics Reports*, 729:1–81, 2017.

[20] Mikhail Polyanskiy. MS Windows NT refractive index database, 2008.

[21] D. G. Rabus. *Integrated Ring Resonators*. Springer, https://link.springer.com/content/pdf/10.1007%2F978-3-540-68788-7.pdf, 1 edition, 2007.

[22] W. J. Riley. *Handbook of Frequency Stability Analysis*. Stable32 and Hamiltan Technical Services, first edition edition, 2007.

[23] Karsten Rottwitt and Peter Tidemand-Lichtenberg. *Nonlinear Optics: Principles and Applications*. CRC Press, 2014.

[24] Thorlabs. MS Windows NT fabry-perot tutorial: Spatial mode structure.

[25] Toptica Photonics. *Tunable Diode Lasers*, 01 2017.

[26] Vien Van. *Optical Microring Resonators*. Boca Raton, CRC Press, first edition edition, 2016.

[27] Zhichao Ye, Krishna Twayana, Peter A. Andrekson, and Victor Torres-Company. High-q si3n4 microresonators based on a subtractive processing for kerr nonlinear optics. *Opt. Express*, 27(24):35719–35727, Nov 2019.

Appendix

Appendix A: Wave Propagation in Waveguides

The propagation of electromagnetic waves in dielectric isotropic materials can be described through Maxwell's equations

$$\nabla \times \mathbf{E}(\mathbf{r},t) = -\frac{\partial \mathbf{B}(\mathbf{r},t)}{\partial t}, \qquad (7.1a) \qquad \nabla \cdot \mathbf{B}(\mathbf{r},t) = 0, \qquad (7.1c)$$

$$\nabla \times \mathbf{H}(\mathbf{r},t) = \frac{\partial \mathbf{D}(\mathbf{r},t)}{\partial t}, \qquad (7.1b) \qquad \nabla \cdot \mathbf{D}(\mathbf{r},t) = 0. \qquad (7.1d)$$

For nonmagnetic materials the constitutive relations are given by the displacement vector field $\mathbf{D}(\mathbf{r},t) = \epsilon_0 \mathbf{E}(\mathbf{r},t) + \mathbf{P}(\mathbf{r},t)$ and the magnetic field $\mathbf{B}(\mathbf{r},t) = \mu_0 \mathbf{H}(\mathbf{r},t)$. Taking the curl of $\nabla \times \mathbf{E}$ and inserting the expression for $\mathbf{H}(\mathbf{r},t)$ and $\mathbf{D}(\mathbf{r},t)$ the equation becomes

$$\nabla \times \nabla \times \mathbf{E}(\mathbf{r},t) = -\left(\frac{1}{c^2}\epsilon_0 \frac{\partial^2 \mathbf{E}(\mathbf{r},t)}{\partial t^2} + \mu_0 \frac{\partial^2 \mathbf{P}(\mathbf{r},t)}{\partial t^2}\right). \qquad (7.2)$$

The polarisation can be rewritten in order to include the nonlinear interactions between light and matter in the materials. This is done using a perturbation series, $\mathbf{P}(\mathbf{r},t) = \sum_{k=1}^{\infty} \mathbf{P}^{(k)}(\mathbf{r},t)$ which can be inserted into Eqn. (7.2) which then becomes the nonlinear wave equation in the time domain,

$$\nabla\times\nabla\times\mathbf{E}(\mathbf{r},t)+\frac{1}{c^2}\frac{\partial^2}{\partial t^2}\int_{-\infty}^{\infty}\left(1+\chi^{(1)}\right)\mathbf{E}(\mathbf{r},\omega)e^{-i\omega t}d\omega = -\mu_0\frac{\partial^2}{\partial t^2}\mathbf{P}^{(\mathrm{NL})}(\mathbf{r},t). \quad (7.3)$$

$\mathbf{P}^{(\mathrm{NL})}(\mathbf{r},t) = \sum_{k=2}^{\infty} \mathbf{P}^{(k)}(\mathbf{r},t)$ is the nonlinear induced polarization. [...] In the frequency domain Eqn. (7.3) translates into

$$\nabla \times \nabla \times \mathbf{E}(\mathbf{r},\omega) = \frac{\omega^2}{c^2}\mathbf{E}(\mathbf{r},\omega) + \mu_0 \omega^2 \mathbf{P}(\mathbf{r},\omega). \qquad (7.4)$$

In the time domain, the field of quasi-monochromatic waves consists of one or more carrier waves multiplied with a slowly varying envelope. [rewrite...?]

$$E(r,\omega) = \frac{1}{2}\left(E^0_{\omega_0} e^{-i\omega_0 t} + c.c\right). \tag{7.5}$$

The linear and nonlinear polarisation can be written as separate fields in a similar form as the electric field. If we only consider positive frequencies the nonlinear wave equation in the frequency domain becomes

$$\nabla\times\nabla\times E^0_{\omega_0}(r,\omega-\omega_0) = \frac{\omega^2}{c^2}E^0_{\omega_0}(r,\omega-\omega_0)+\mu_0\omega^2\left[(P^0_{\omega_0})^L(r,\omega-\omega_0)+(P^0_{\omega_0})^{NL}(r,\omega-\omega_0)\right]. \tag{7.6}$$

Assuming that the material is homogeneous allows us to write $\nabla\times\nabla\times E = -\nabla^2 E$ and Eqn. (7.6) then becomes:

$$\left(\nabla^2 + \frac{\omega^2}{c^2}\left(1+\chi^{(1)}\right)\right)E^0_{\omega_0}(r,\omega-\omega_0) = -\mu_0\omega^2(P^0_{\omega_0})^{NL}(r,\omega-\omega_0), \tag{7.7}$$

where the linear part of the polarisation have been rewritten using $\epsilon_0\mu_0 = 1/c^2$. The nonlinear polarisation can in many cases, such as the optical Kerr effect and four wave mixing, be written as an effective linear polarisation:

$$(P^0_{\omega_0})^{NL}(r,\omega-\omega_0) = \epsilon_0 K\chi^{(3)}E^0_{\omega_1}E^0_{\omega_2}E^0_{\omega_0} = \epsilon_0\tilde{\chi}^{(1)}E^0_{\omega_0}, \tag{7.8}$$

where $\tilde{\chi}^{(1)}$ is the effective first-order nonlinearity. Using this, Eqn. (7.7) becomes:

$$\left(\nabla^2 + \frac{\omega^2}{c^2}\left(1+\chi^{(1)}+\tilde{\chi}^{(1)}\right)\right)E^0_{\omega_0}(r,\omega-\omega_0) = 0. \tag{7.9}$$

The nonlinear wave equation can be derived for a field propagating in a homogeneous waveguide by assuming that the amplitude of the field can be separated into an envelope $\mathcal{A}(\omega-\omega_\sigma)$ and a radial distribution $R(r)$,

$$E_{\omega_0}(r,\omega-\omega_0) = \mathcal{A}(\omega-\omega_0)R(r)e^{i\beta_0 z}. \tag{7.10}$$

Inserting the electric field in Eqn. (7.10) into Eqn. (7.9):

$$\left(\nabla^2 + \frac{\omega^2}{c^2}\left(1+\chi^{(1)}+\tilde{\chi}^{(1)}\right)\right)\mathcal{A}(\omega-\omega_0)R(r)e^{i\beta_0 z} = 0. \tag{7.11}$$

In order to solve Eqn. (7.11) we apply seperation of variable in order to separate the radial and longitudinal dependencies:

$$\left[-\nabla^2_\perp R(r) + \frac{\omega^2}{c^2}(1+\chi^{(1)}+\tilde{\chi}^{(1)})R(r)\right]\frac{1}{R(r)} = \frac{1}{\mathcal{A}e^{i\beta_0 z}}\nabla^2_z(\mathcal{A}e^{i\beta_0 z}). \tag{7.12}$$

The RHS now only depends on r whereas the LHS only depends on z. This means we can set both of them equal to some constant $\tilde{\beta}^2$ such that we obtain two equations:

$$\left[-\nabla_\perp^2 R(r) + \frac{\omega^2}{c^2}(1+\chi^{(1)}+\tilde{\chi}^{(1)})R(r)\right]\frac{1}{R(r)} = \tilde{\beta}^2, \tag{7.13}$$

$$\frac{1}{\mathcal{A}e^{i\beta_0 z}}\nabla_z^2(\mathcal{A}e^{i\beta_0 z}) = \tilde{\beta}^2. \tag{7.14}$$

From Eqn. (7.13) the transverse mode can be defined through a solution of:

$$\left[-\nabla_\perp^2 R(r) + \frac{\omega^2}{c^2}(1+\chi^{(1)}+\tilde{\chi}^{(1)})R(r)\right] - \tilde{\beta}^2 R(r) = 0, \tag{7.15}$$

in which we will neglect $\tilde{\chi}^{(1)}$ assuming that the nonlinearity does not affect the mode $R(r)$. The mode problem can be solved in order to find $R(r)$ and $\beta(\omega)$ by considering the Laplacian operator in cylindrical coordinates $\frac{\partial^2}{\partial r^2} + \frac{1}{r}\frac{\partial}{\partial r} + \frac{1}{r^2}\frac{\partial^2}{\partial \theta^2}$ and letting the solutions be separable in radial and azimuthal dependence:

$$\phi(r,\theta) = R(r)\begin{Bmatrix} cos(m\theta) \\ sin(m\theta) \end{Bmatrix}. \tag{7.16}$$

In a step index fiber with homogeneous layers the problem will take the form $\nabla_\perp^2\phi + (k^2 n_i^2 - \beta^2)\phi = 0$, where n_i $(i = 0, 1)$ is the refractive in the cladding and core, respectively. Inserting Eqn. (7.16) into the wave equation along with the expression for the Laplacian operator we obtain:

$$\frac{\partial^2 R}{\partial r^2} + \frac{1}{r}\frac{\partial R}{\partial r} - \frac{1}{r^2}m^2 R + (k^2 n^2 - \beta^2)R = 0, \tag{7.17}$$

which is a Bessel differential equation when $\beta < kn$ and a modified Bessel differential equation when $\beta > kn$. Applying boundary conditions at $r- > \infty$ and $r = 0$ the modes can be found as solutions from:

$$u\frac{J_{l+1}(u)}{J_l(u)} = v\frac{K_{l+1}(v)}{K_l(v)}, \tag{7.18}$$

where J_l and K_l are the Bessel and modified Bessel, respectively.

We consider a simple unperturbed waveguide structure in which the eigenmode shape R and corresponding propagation constant β are known. A perturbation to such a structure can be expressed in terms of a change on the relative dielectric constant $\Delta\epsilon_r$ replacing ϵ_r with $\epsilon_r + \Delta\epsilon_r$ where $\Delta\epsilon_r$ is the uniform perturbation along z ($\Delta\epsilon_r = \tilde{\chi}^{(1)}$). In the same manner as we introduced $\epsilon_r \to \epsilon_r + \Delta\epsilon_r$ we will also have to introduce $R + \Delta R$ and $\beta + \Delta\beta$.

Beginning with Eqn. (7.13), neglecting the higher-order perturbation terms:

$$\nabla_\perp^2(R+\Delta R) + [(\epsilon_r + \Delta\epsilon_r)k^2 - (\beta - \Delta\beta)^2](R+\Delta R) = 0, \tag{7.19}$$

$$\nabla^2 \Delta R + \epsilon_r k^2 \Delta R + \Delta\epsilon_r k^2 R - \beta^2 \Delta R - 2\beta\Delta\beta R = 0. \tag{7.20}$$

We then multiply with the complex conjugate of the transverse mode R:

$$\nabla^2 \Delta R R^* + \epsilon_r k^2 \Delta R R^* + \Delta\epsilon_r k^2 |R|^2 - \beta^2 \Delta R R^* - 2\beta\Delta\beta |R|^2 = 0, \tag{7.21}$$

and integrate over the entire waveguide cross section:

$$2\beta\Delta\beta \int_A |R|^2 da = \int_A \Delta\epsilon_r k^2 |R|^2 da + \int_A \left[(\nabla_\perp^2 \Delta R) R^* + \epsilon_r k^2 \Delta R R^* - \beta^2 \Delta R R^* \right] da. \tag{7.22}$$

If we multiply the complex conjugate of the transverse wave equation by ΔR, $\Delta R(\nabla_\perp^2 R^* + [\epsilon_r^* k^2 - \beta^{*2}]R) = 0$ and put it back into Eqn. (7.22):

$$2\beta\Delta\beta \int_A |R|^2 da = \int_A \Delta\epsilon_r k^2 |R|^2 da$$
$$+ \int_A \left[(\nabla_\perp^2 \Delta R) R^* - \Delta R (\nabla_\perp^2 R^*) + \Delta R k^2 (\epsilon_r - \epsilon_r^*) R^* - \Delta R (\beta^2 - \beta^{*2}) R^* \right] da, \tag{7.23}$$

where we have subtracted the complex conjugate of the wave equation multiplied with ΔR in order to show:

1. $\Delta R \nabla_\perp^2 R^* + \Delta R \epsilon_r^* k^2 R^* - \Delta R \beta^{*2} R^* = 0$
2. $(\nabla_\perp^2 \Delta R) R^* - \Delta R \nabla_\perp^2 R^* + \Delta R (\epsilon_r - \epsilon_r^*) R^* - \Delta R (\beta^2 - \beta^{*2}) R^*$

Now, since ϵ_r and β are purely real it reduces to:

$$2\beta\Delta\beta \int_A |R|^2 da = \int_A \left[(\nabla_\perp^2 \Delta R) R^* - (\nabla_\perp^2 R^*) \Delta R \right] da + \int_A \Delta\epsilon_r k^2 |R|^2 da. \tag{7.24}$$

According to Green's theorem the first term on the RHS equals 0 which leaves us with:

$$2\beta\Delta\beta \int_A |R|^2 da = \int_A \Delta\epsilon_r k^2 |R|^2 da, \tag{7.25}$$

from which we find:

$$\Delta\beta = \frac{k^2}{2\beta} \frac{\int_A \Delta\epsilon_r |R|^2 da}{\int_A |R|^2 da}, \tag{7.26}$$

with $k = \omega/c$ and $\beta = k n_{eff}$. From Eqn. (7.25) we see that a small change in ΔR has no effect on the propagation constant since assuming a purely real permittivity (hence a real propagation constant) the change in propagation constant is solely determined by $\Delta\epsilon_r$. This implies that Eqn. (7.14) describes the propagation in the waveguide. Writing out the the equation results in:

$$\frac{\partial^2 A}{\partial z^2} + 2i\beta_0 \frac{\partial A}{\partial z} - \beta_0^2 A + \tilde{\beta}^2 A = 0. \tag{7.27}$$

A pulse propagating in the z-direction can be written as a complex-valued slowly-varying envelope function $A_{\omega_\sigma}(z,t)$ of the electric field. A slowly-varying envelope function changes very little over lengths comparable to the wavelength satisfying:

$$\left|\frac{\partial^2 A_{\omega_\sigma}}{\partial z^2}\right| \ll \left|k_\sigma \frac{\partial A_{\omega_\sigma}}{\partial z}\right|. \tag{7.28}$$

Applying the slowly-varying envelope approximation (SVEA):

$$\tilde{\beta} = \beta(\omega) + \Delta\beta \approx \beta_0 + \beta_1(\omega - \omega_0) + \frac{1}{2}\beta_2(\omega - \omega_0)^2 + \Delta\beta, \tag{7.29}$$

with $\Delta\beta$ as defined in Eqn. (7.26) where $\tilde{\chi}^{(1)} = \Delta\epsilon_r$ and $\beta_0 = \beta(\omega_0)$, $\beta_1 = \left.\frac{\partial\beta}{\partial\omega}\right|_{\omega_0}$ and $\beta_2 = \left.\frac{\partial^2\beta}{\partial\omega^2}\right|_{\omega_0}$. Using the approximation:

$$\beta_0^2 - \tilde{\beta}^2 \approx 2\beta_0(\beta_0\tilde{\beta}), \tag{7.30}$$

we get the expression:

$$i\frac{\partial A}{\partial z} + \left(\beta_1(\omega - \omega_0) + \frac{1}{2}\beta_2(\omega - \omega_0)^2 + \Delta\beta\right)A = 0. \tag{7.31}$$

Using the Fourier transform $\omega^n F(\omega) \leftrightarrow i^n \frac{\partial^n}{\partial t^n}$ the Eqn. (7.31) is translated into the time domain:

$$\frac{\partial A}{\partial z} + \beta_1\frac{\partial A}{\partial t} + \frac{i}{2}\beta_2\frac{\partial^2 A}{\partial t^2} - i\Delta\beta A = 0, \tag{7.32}$$

where β_1 is the inverse group velocity, β_2 the group velocity dispersion and $\Delta\beta$ is the change in the propagation constant.

A pulse propagating through a waveguide will be subject to dispersion through the intensity dependent refractive index. This can be accounted for by writing the change in the propagation constant as:

$$\Delta\beta = \frac{\omega n_2^I}{c}\frac{P}{A_{eff}}, \tag{7.33}$$

with n_2^I being the intensity dependent refractive index, P the power and A_{eff} the effective area. This last rewriting allows us to rewrite the last term in the LHS in Eqn. (7.32):

$$i\Delta\beta A = i\gamma|A|^2 A, \tag{7.34}$$

where $P = |A|^2$ and $\gamma = 2\pi n_2/\lambda A_{eff}$. Finally, introducing a coordinate system moving with the group velocity reduces Eqn. (7.32) to:

$$\frac{\partial A}{\partial z} - \frac{i}{2}\beta_2\frac{\partial^2 A}{\partial t^2} - i\gamma|A|^2 A = 0. \tag{7.35}$$

This equation is known os the *Nonlinear Schrödinger Equation* (NLSE). The second term on the RHS is responsible for the group velocity dispersion (GVD) and the last term on the RHS is the term responsible for the nonlinearity (the Kerr effect).

In a lossy fibre the intrinsic loss, α, can be accounted for by adding an extra term. The term can be included in $\Delta\beta$ by substituting:

$$\Delta n = n_2|E|^2 \rightarrow \Delta n = n_2|E|^2 + \frac{i}{2k_0}\alpha, \tag{7.36}$$

which then would show up in the expression for $\Delta\beta$ as:

$$\Delta\beta = \frac{\omega}{c}\left(n_2^I \frac{P}{A_{eff}} + i\alpha\right) \tag{7.37}$$

Including this extra term in the NLSE the equation then becomes:

$$\frac{\partial A}{\partial z} - \frac{i}{2}\beta_2 \frac{\partial^2 A}{\partial t^2} - i\gamma|A|^2 A - \frac{\alpha}{2} = 0. \tag{7.38}$$

Appendix B: Fit Parameters for all N

N	FSR [GHz]	D_2 [MHz]	β_2 [ps^2/km]	σ_{res}	Estimated cavity length [cm]
1	100.2882 ± 0.0001	0.619 ± 0.003	-65.2 ± 0.4	24.0015	154.7
2	100.2882 ± 0.0001	0.619 ± 0.003	-65.2 ± 0.4	24.1045	77.3
3	100.2882 ± 0.0001	0.618 ± 0.004	-65.1 ± 0.4	24.5946	51.6
4	100.2882 ± 0.0001	0.617 ± 0.004	-65.0 ± 0.4	25.4800	38.7
5	100.2882 ± 0.0001	0.618 ± 0.004	-65.2 ± 0.4	26.7465	30.9
6	100.2882 ± 0.0002	0.616 ± 0.004	-64.9 ± 0.4	28.5150	25.8
7	100.2882 ± 0.0002	0.615 ± 0.004	-64.8 ± 0.5	31.4760	22.1
8	100.2882 ± 0.0002	0.613 ± 0.004	-64.6 ± 0.5	31.7724	19.3
9	100.2882 ± 0.0002	0.613 ± 0.005	-64.6 ± 0.5	34.5573	17.2
10	100.2883 ± 0.0002	0.618 ± 0.005	-65.1 ± 0.5	34.1549	15.5
11	100.2883 ± 0.0002	0.614 ± 0.005	-64.7 ± 0.5	33.9904	14.1
12	100.2884 ± 0.0002	0.612 ± 0.005	-64.7 ± 0.5	32.8462	12.9